



**UT
CB**



Technical University of Civil Engineering Bucharest

**Faculty of
Geodesy**

Revista de Geodezie, Cartografie și Cadastru

***Journal of Geodesy,
Cartography and Cadastre***

No. 9

Bucharest 2018

ISSN: 1454-1408

*Revista de Geodezie,
Cartografie și Cadastru*

*Journal of Geodesy,
Cartography and Cadastre*

No. 9

București 2018
ISSN: 1454-1408

Editorial Board

- Prof. PhD. Habil. Eng. **Ana-Cornelia BADEA** - President
- Assoc. Prof. PhD. Eng. **Adrian SAVU** - Editor in chief

Headings coordinators

- Assoc. Prof. PhD. Eng. **Caius DIDULESCU**
- Assoc. Prof. PhD. Eng. **Octavian BĂDESCU**
- PhD. **Ioan STOIAN**
- PhD. **Vasile NACU**

Online Editor

- Assoc. Prof. PhD. Eng. **Aurel Cătălin Florentin NEGRILĂ**

Editorial secretary

- Assist. Prof. PhD. **Paul DUMITRU**

Scientific Committee

- Prof. PhD. Eng. **Petre Iuliu DRAGOMIR**
- Prof. PhD. Eng. **Dumitru ONOSE**
- Prof. PhD. Eng. **Iohan NEUNER**
- Prof. PhD. Eng. **Constantin COȘARCĂ**
- Prof. PhD. Habil. Eng. **Gheorghe BADEA**
- Prof. PhD. Habil. Eng. **Carmen GRECEA**
- Prof. PhD. Habil. Eng. **Sorin HERBAN**
- Prof. PhD. Eng. **Maricel PALAMARIU**
- Prof. PhD. Eng. **Cornel PĂUNESCU**
- Prof. PhD. Eng. **Constantin BOFU**
- Assoc. Prof. PhD. Eng. **Livia NISTOR**
- Assoc. Prof. PhD. Eng. **Constantin CHIRILĂ**

* The author(s) of each article is/are solely responsible for the content.

Table of Contents

Monitoring of supporting structures with profile laser scanning

Florian Schill, Andreas Eichhorn 1

Position Determination of a Moving Reflector in Real Time by Robotic Total Station Angle Measurements

Gabriel Kerekes, Volker Schwieger 13

Aspects of Intra-Frame Velocity (Deformation) Models for the United States National Spatial Reference System in 2022

Daniel Roman 19

Monitoring of the Church Tower in Herrenberg with Low-Cost GNSS

Li Zhang, Iuliana-Madalina Ionescu, Volker Schwieger 23

Tri-Axial Accelerometer Calibration for Leveling

Tomas Thalmann, Hans Neuner 29

Solar potential assessment and its feasibility using semi-automatic feature extraction and pyranometer for smart cities

Mudit Kapoor, Rahul Dev Garg 37

Monitoring of supporting structures with profile laser scanning

Florian Schill¹, Andreas Eichhorn

Received: September 2018 / Accepted: October 2018 / Published: December 2018
© Journal of Geodesy, Cartography and Cadastre/ UGR

Abstract

This paper presents the evaluation of measurements on bridge structures with a profile scanner and shows that existing concepts of classical monitoring measurements can be extended with the use of profile laser scanning.

The contact-free acquisition method of profile laser scanners reduces the expense for personnel and instrumentation compared to conventional sensors used for the monitoring of civil engineering structures. It furthermore enables the measurement of non-accessible areas of the monitored supporting structures. In addition, the availability of information along an entire structural profile can be used to flexibly deal with a wide variety of problems. With a measurement rate of at least 50 Hz, typical structural deformation signals can be recorded and sufficient data can be collected to characterize the underlying deformation processes dependably.

Overall, an automated and efficient spatio temporal processing scheme is presented, which is based on the discrete wavelet transform. With this signal analysis tool outliers are detected and eliminated, but furthermore an automated structural analysis based on the details of the supporting structures surface is realized.

In addition to the derivation of deformations, a quality assessment with comprehensive integration of the redundant measurement information is possible as an in-situ uncertainty determination.

Keywords

Laser scanning, discrete wavelet transform, monitoring, supporting structures, bridges, time series analysis, spatio temporal processing scheme

1. Motivation

A fundamental objective of geodetic monitoring is the acquisition of geometric object changes under the influence of loads [1]. In particular, the monitoring of supporting structures is of great importance, since the structural members as a whole system of all supporting elements of a construction or engineering structure are responsible for its stability.

Since engineering structures are often systems that are capable of vibration and the predominant part of all load factors has a dynamic character, the focus of corresponding monitoring measurements is on the collection of temporally variable structural deformations. These deformations can only be recorded with sensors that provide a high temporal resolution.

Up-to-date the primary components of such measuring concepts are acceleration sensors, inductive displacement sensors and strain gauges. Although these sensors provide highly accurate data that is optimally adapted to the application, they must be mounted on the measuring object producing an enormous workload. Furthermore, inaccessible areas that do not allow the mounting of these sensors are particularly problematic. In general, the measurement information obtained in this way is only available at discrete object points and cannot be interpreted without appropriate prior knowledge about the supporting structure.

The purpose of this paper is to demonstrate that profile scanners have the potential to solve the problems discussed above and to complement existing measurement concepts. Due to the repeated acquisition along a profile, the measurement data possesses both temporal and spatial resolution, which can be ideally combined with the measurement information obtained at discrete points.

In the following chapter the measurement system is introduced and the most important parameters are explained.

Chapter 3 shows how the derivative of spatially distributed time series is carried out in the context of space-temporal processing using the temporal and spatial resolution of the profile scanner.

¹ Dr.-Ing. Florian Schill
Technische Universität Darmstadt
FG Geodätische Messsysteme und Sensorik
Institut für Geodäsie
Franziska-Braun-Straße 7
64287 Darmstadt
schill@geod.tu-darmstadt.de

The basic principles are further deepened with practical examples in Chapter 4 and 5. The main focus lies on railway bridges, whereby the examples differ significantly in the deformation signals and bridge characteristics that occur. This shows the potential of the profile scanner for the monitoring of supporting structures and demonstrates the universal applicability of the developed processing scheme.

2. Measurement system based on a profile scanner

The profile scanner used in this investigation is a phase-based Zoller+Fröhlich Profiler 9012. It is a pure 2D scanner, see Figure 1. All adapters for using it in the area of monitoring are proprietary developments (tripod and targeting adaptor). Due to the special type of adaptation both vertical and horizontal measurements are possible, but also in the entire angle range in between. Since the profile scanner is equipped with a GPS receiver, a time stamp can be calculated for each individual point. The maximum measurement distance is specified by the manufacturer with 119 m. With a data recording rate of up to 1 million points per second, measuring speeds of 50, 100 or 200 profiles per second are possible [2].



Fig. 1 Profile scanner under a railway bridge.

In Figure 1, a schematic measurement profile and the corresponding coordinate axes are displayed together with the profile scanner. Accordingly, Figure 2 shows the y-/z-measurement plane of the profile scanner with approximately 20.000 measuring points in one measurement profile.

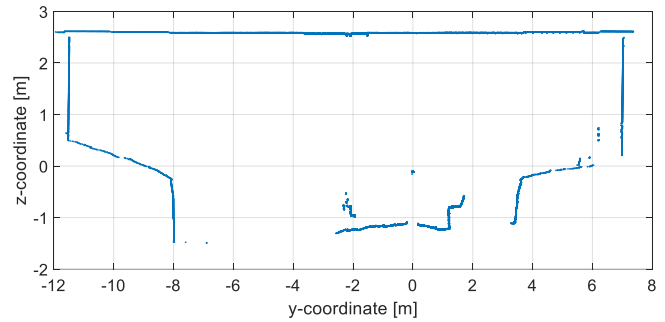


Fig. 2 Raw measurement profile with approximately 20.000 points.

3. Spatio temporal processing scheme

The profile scanner determines a spatial and temporal component for every measured point, which corresponds to a spatio temporal acquisition of the structural members. However, the original measured values of the profile scanner are not directly usable for the monitoring of supporting structures, as they are not directly accessible and on the other hand not reproducible [3].

The measured values (organized in profiles) must therefore be analyzed in the context of the structural surface and local conditions. Due to the large number of measurement profiles belonging to a scan, this analysis has to be automated for efficiency reasons.

For this purpose, a universally applicable processing scheme has been developed, of which the flowchart is depicted in Figure 3. The scheme subdivides into three parts:

- The automatic analysis of the measurement profiles,
- The profile-wise spatial processing,
- The scan-wise temporal processing.

The first step is the **automatic analysis of the measurement profiles** with the objective to eliminate all measured points not belonging to the structural surface and to segment the complex measurement profiles into simpler segments. This part of the spatio temporal processing scheme is presented in detail in [3] and [4].

Based on those simplified profile segments a **profile-wise spatial processing** can be implemented for example as an approximation with spatial clustering, B-spline functions [5], wavelets [6] or others. Those spatial processing approaches are extensively discussed in [3].

The choice of the different processing approaches depends heavily on the structure to be examined. In principle, it can be differentiated into two categories: smooth surfaces, as in the investigations of wind turbines in [7] or structured object surfaces, which can occur at steel bridge structures [4].

In case of smooth surfaces, the selection of the evaluation strategy is relatively free and depends mainly on the evaluation target, such as the use of continuous functions for the determination of eigenmodes or the formation of spatial cluster for the calculation of eigenfrequencies of the supporting structure.

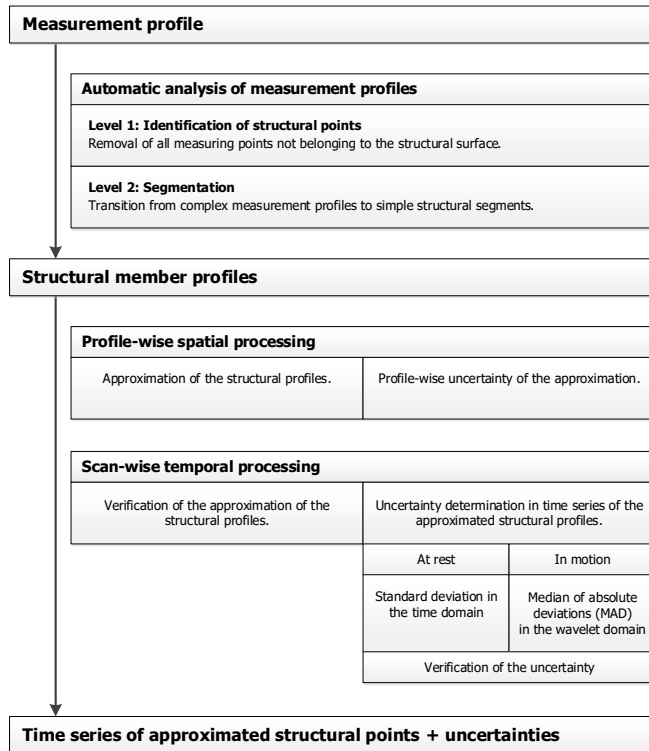


Fig. 3 Spatio temporal processing scheme.

Independent of the profile-wise spatial processing method, after the following **scan-wise temporal processing**, the final results are time series of approximated structural points and corresponding uncertainties. These can be used as a starting point for investigations that optimally capture the deformation behavior both in terms of space and time, thus forming the basis for the monitoring of supporting structures with a profile scanner.

In the following the application of the spatio temporal processing scheme will be reviewed in detail with two very different examples, which vary not only in the before mentioned difference of the supporting structures surface, but also in the occurring deformation signals:

- **Example 1:** A steel bridge with a heavily structured surface (Chapter 4) whereas the analysis concentrates on quasi static deformations.
- **Example 2:** A steel bridge with a smooth surface (Chapter 5) whereas the analysis concentrates on the dynamic deformation component.

4. Example 1: Single-tracked railway bridge over the Flanitz at Klingenbrunn

The examined engineering structure is an over one hundred year old single-tracked railway bridge with a span of just under 20 m. The main beams are designed as solid steel girders and only sit on the two abutments, see Figure 4. The bridge was subsequently extended by two footpaths, which are connected with the actual bridge only at the abutments.



Fig. 4 Side view of the single-tracked railway bridge.

The measurements took place during ongoing railway operations. The trains were Regio-shuttle RS1 with an empty weight of approx. 41 tones and a speed at the bridge crossing of approx. 30 km/h. The individual passages are therefore distinguished mainly by the direction of travel and the number of used wagons.

With the profile scanner two different measurement configurations have been recorded which will be reviewed in the following:

- Along the bridge axis on the main girders (4.1),
- Perpendicular to the bridge axis in the middle of the bridge (4.2).

4.1 Analysis of the main girders along the bridge axis

Figure 5 shows a schematic longitudinal section through the bridge structure along one main girder. Since the two main girders are identical in construction, this figure is representative for both of them. The main girders consist of two steel full-wall beams, which are connected in the middle of the bridge. To connect and stabilize the two parts of the main girders they are additionally stiffened to the middle of the bridge. This is greatly exaggerated in Figure 5 by the increasing thickness of the main girder.

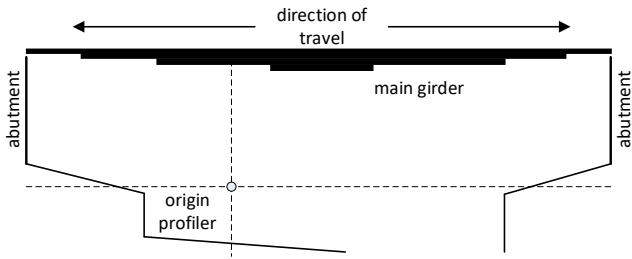


Fig. 5 Schematic longitudinal section through the main girder of the single-tracked railway bridge.

In Figure 6 the result of the automatic analysis of an exemplary measurement profile is shown for the first configuration. According to the statements of Chapter 3, the automatic analysis of the measurement profiles removes erroneous measurements as well as disturbing structural details. Following this, the structure of the surface is segmented based on its details. In Figure 6 the measurement points belonging to the resulting structural segments are highlighted in color from the original profile measurement (in blue). In this case, the surface structure of the main girder leads to a segmentation into eight parts.

The results of the automatic analysis of the measuring profiles are so-called structural segments, which have to be further processed for the spatio temporal determination of the vertical deformation, see Figure 3. In this case an approximation with continuous functions such as B-splines or wavelets is not useful, due to the spatially limited segments. Therefore a spatial clustering is carried out in the following.

The measuring points within such a spatial unit are jointly processed with the aim of producing a derived representative per cluster. With this simple definition, spatial clustering is an almost universally usable processing approach, whose computing power is very low, especially if, as in this example, the cluster representative is formed from the mean value.

The definition of the cluster size is realized using the same angle ranges. Thus, in this case 71 clusters are created, which are highlighted in Figure 7 in color. The spatial extent of the clusters vary between 0.1 m and 1.4 m, but the number of measuring points included in every cluster is almost constant. This offers the advantage that the measuring time for all clusters is about the same duration and thus the uncertainty due to the sequential measurement has the same magnitude.

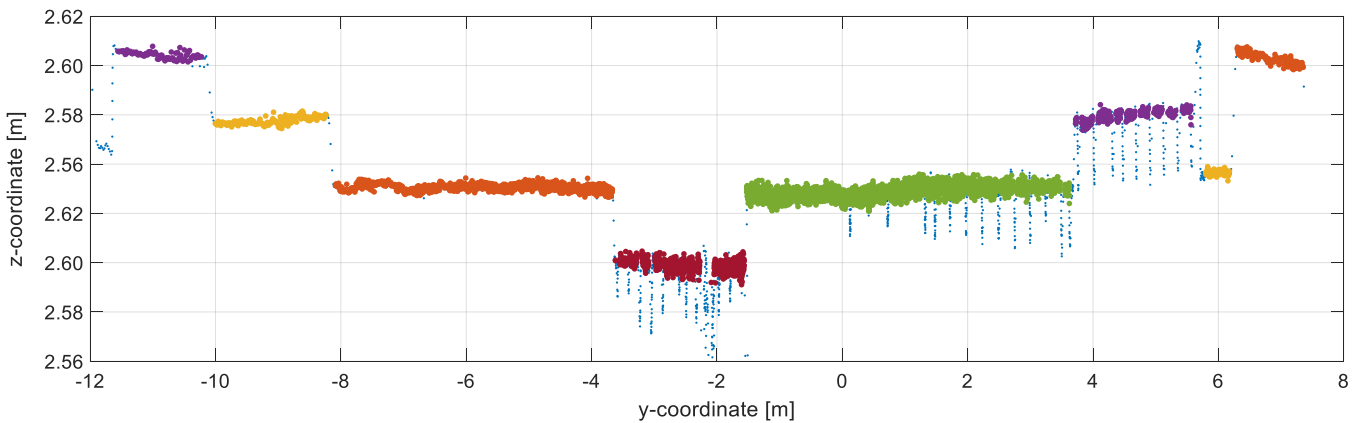


Fig. 6 Automatic segmented measuring profile along a main girder.

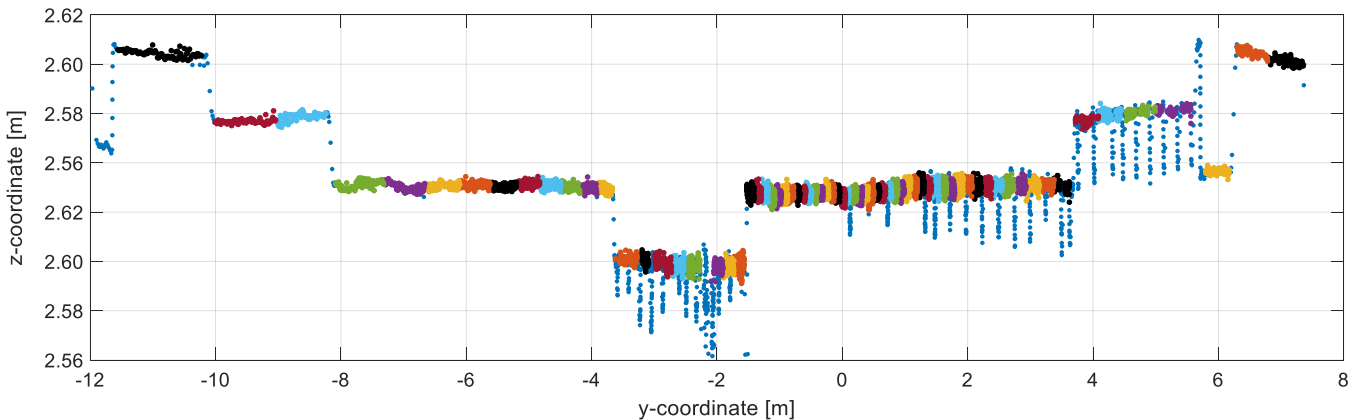


Fig. 7 Spatial clustering based on the automatic segmentation.

By processing the spatially distributed clusters, the transition to a spatio temporal representation is created, see Figure 8. The top chart shows the time series of a cluster representative in the middle of the structure.

In the six diagrams underneath exemplary epochs of the space-time representation are shown on the right side. On the left side, the corresponding position of the train is shown on the bridge. The position at which the time series shown in the top chart was evaluated, is additionally marked with a blue arrow.

The assignment of the cluster representatives within the epochs of the spatial representation (right side) to the bridge structure in Figure 7 is possible on the basis of the consistent coloring of the clusters and their representatives. The temporal mapping of the six spatial representations can be done using the time stamps or the corresponding coloring of the markers in the top chart.

In combination with the situational sketches, the top-level diagram is used to illustrate the general sequence of the train crossing:

The load of the wagons is divided between the two bogies, so that the double wagon shown in this example has four load points, the middle two of which are so close that these two can be combined. The following considerations therefore assume three load points with different loads. Since the distance of the bogies with 17 m is almost as large as the span of the main beams with 19.6 m, there is usually only one load point on the bridge at the same time.

Accordingly, the time series of the z-coordinate of the cluster representative in the upper diagram in Figure 8 shows three local minima. The maximum deflection (middle minimum) occurs when the rear bogie of the first wagon is located on the bridge together with the front bogie of the second wagon (middle load point). The other two local minima are caused by the other bogies of the front or rear wagon.

In the six epochs depicted in Figure 8, the relative changes of the bridge form are illustrated. This shows that the bending line, as expected, takes on a different shape depending on the position of the bogies of the wagons on the bridge:

1. The green epoch shows the situation after the front bogie of the first wagon has been driven onto the bridge. The amplitude of the bending line is low and the shape is asymmetric according to the train position.
2. At the time of the blue epoch, the first bogie of the first wagon is located directly in the middle of the bridge, which at this time is the first local minimum. The shape of the bending line is symmetrical around the center of the bridge with a maximum amplitude of 5 mm.

3. In the turquoise epoch the first partial relief of the bridge is shown. The first and second load points are symmetrical to the center of the bridge at the two bridge edges, which also creates a symmetrical bend line characterized by two load points. An almost constant deflection of 2 mm is achieved over a total area of about 9 m.
4. The black epoch shows the maximum load on the bridge through the central load point (two bogies). The maximum deflection of nearly 8 mm occurs in the middle of the bridge. However, the load situation corresponds to the blue epoch but with a higher load. In the area of the y-coordinate of 3.5 m, some cluster representatives have a greater deflection than would be expected for a homogeneous bend line. This is the border area of the fourth structural segment from the right, compared to Figure 7.
5. The magenta epoch shows a very asymmetrical bending line, since during the double-load point just leaves the bridge, the last bogie is not yet in the middle of the bridge.
6. The time of the red epoch shows the situation just before the last bogie leaves the bridge. The shape of the bending line is similar to a mirrored version of the green epoch.

The spatio temporal processing allows the acquisition of the entire surface structure within a profile. Therefore it is possible to directly measure the complete bending line, and also to detect deviant behavior of individual profile segments, as seen exemplary in the black epoch in Figure 8.

Such model disruptions can be detected with profile scanner measurements, due to the high spatial resolution. In comparison this is not possible with classical sensors for the monitoring of bridges, because the density of the discrete measuring points is much sparser.

Therefore the decision for those discrete measuring positions has to be planned based on appropriate prior knowledge about the supporting structure or on the theoretical deformation behavior.

The usage of profile scanning has the advantage that there is no need for such a great effort for the measuring planning. On the contrary it offers high flexibility combined with low planning expenses.

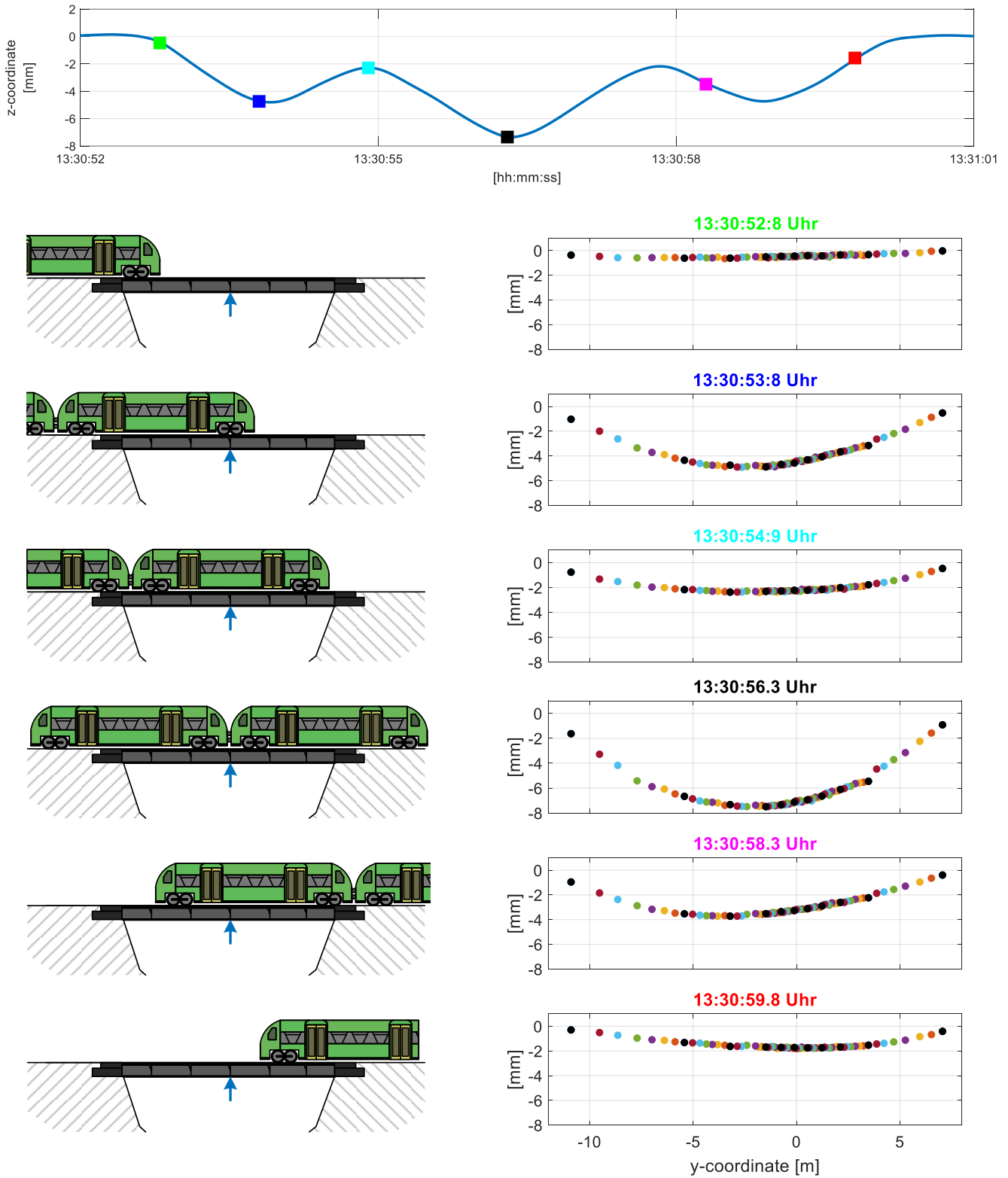


Fig. 8 Spatio temporal representation of a train crossing with two wagons. Top graph: Time series of a cluster representative for the classification of the individual epochs of spatial representation. The remaining six illustrations correspond to the spatial representation of a defined point in time during the crossing (epochs).

4.2 Analysis of the main girders perpendicular to the bridge axis

In addition to the evaluations of the vertical component shown in the previous analyses, the horizontal deformation of the bridge can be recorded in particular with the measurement of the configuration 2. The following versions are therefore concerned with the evaluation of this configuration, which was measured perpendicular to the main bridge axis. The focus lies on the simultaneous recording of the horizontal deformation of both main girders.

The position of the bridge in a curve, creates in addition to the vertical deformation also a horizontal deformation of the main girders. This is caused by the combination of the centrifugal force due to the curve position of the bridge and the sine run of the train [8].

To determine the horizontal deformation, a modified automatic analysis of the measuring profiles must be carried out, wherein the analysis focuses on the y-coordinate values. Based on the resulting segmentation, a spatial clustering takes place, the result of which is shown in Figure 9.

Here, too, the cluster definition takes place over the same angle range, so that all clusters contain approximately the same number of measuring points.

For the determination of the horizontal deformation of the two main girders, the blue cluster is selected on the main girder 1 and the orange cluster on the main girder 2 as representative examples. Both cluster have a vertical extension of approx. 0.15 m and include approximately 80 points.

Figure 10 shows the time series of the cluster representatives of the blue and orange cluster from Figure 9. Both time series are divided into three parts: before the crossing, during the crossing and after the crossing, which are visually separated from each other by black lines.

The uncertainty for the y-coordinate of the two cluster representatives can be determined from the cut-outs before and after the crossing (without load) in the time domain. The blue time series results in a standard deviation of approx. 0.13 mm and the orange time series results in a standard deviation of approx. 0.11 mm.

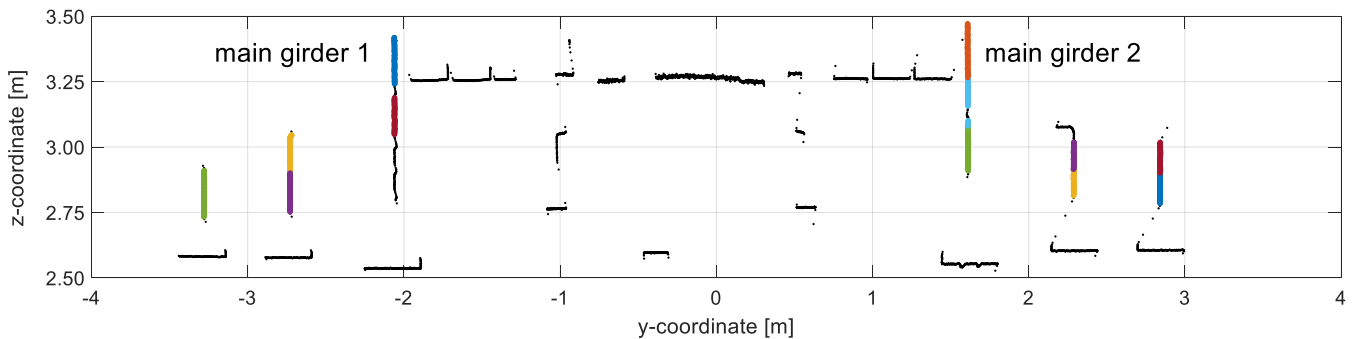


Fig. 9 Spatial clustering based on the automatic segmented profile in configuration 2.

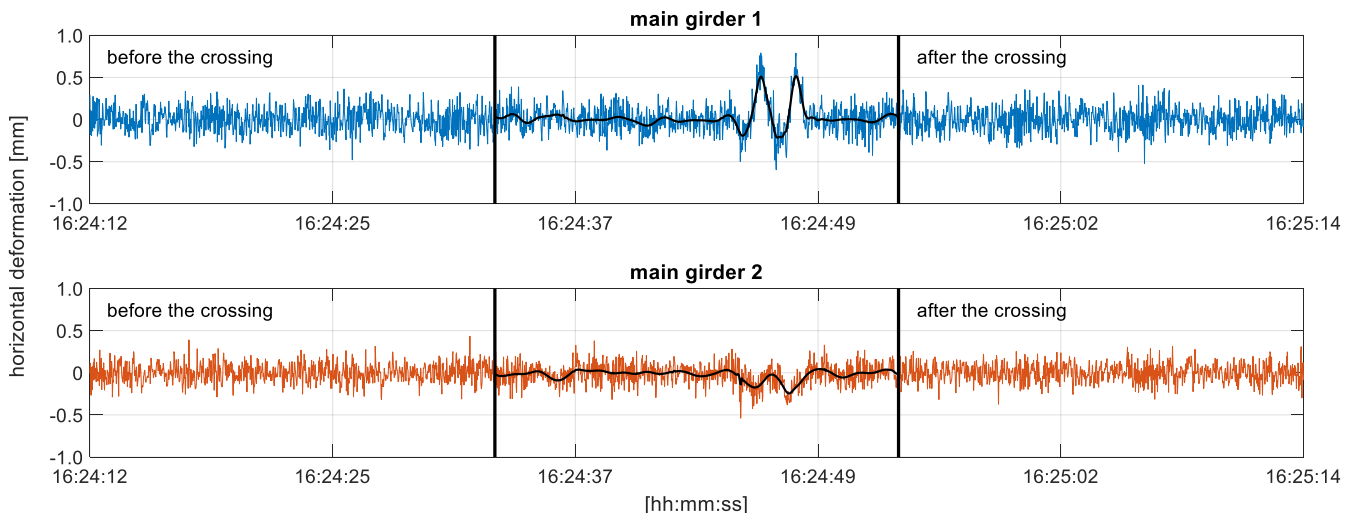


Fig. 10 Time series of the cluster representatives for the blue and orange cluster.

Using these results, the cutout during the crossing is denoised (wavelet denoising) and the result is superimposed on the actual deformation signal in black.

In both time series, the horizontal deformations can be verified which are induced by the forces from the bogies of the train. The main carrier 1 (outside of the curve) has a maximum horizontal deformation of over 0.5 mm at the crossing of both bogies. For the main carrier 2, the magnitude of the horizontal deformation is only just above the noise level. This shows that due to the position in the curve most of the horizontal load rests on the outer track.

Due to the possibility of a combined registration of the vertical (Chapter 4.1) and horizontal deformation of supporting structures, the use of the profile scanner also provides the potential to capture information about the structural behavior in order to improve the planning of large measurement campaigns. For example, it can be preanalyzed whether the lateral deformations of the bridge distorts the results of other sensors culminating in the verification and even correction of the measurements of those sensors, see [9].

5. Example 2: Trough bridge over the Aller

The second monitored engineering structure is a newly built railway bridge over the Aller near Verden (Niedersachsen). The bridge is 380 meters long, consists of seven bridge spans and was executed as a joint less steel bridge. The maximum route speed is 160 km/h.

All measurements took place on the eastern main beam of the bridge in longitudinal direction. The measured bridge span has a length of approx. 50 m, see Figure 11.

In contrast to the single-tracked railway bridge from Chapter 4, the surface of the main beam has no structuring, so that the automatic analysis of the measurement profiles only creates one profile segment.



Fig. 11 Trough bridge over the Aller.

For this reason, all spatial processing methods presented in Chapter 3 are suitable for further analyses.

Figure 12 depicts the results of the spatial clustering and the B-spline approximation for a single measurement profile on the eastern main beam between two supports.

The profile points are divided into 100 spatial clusters and are appropriately colored. The expansion of the spatial cluster is again chosen in such a way that all cluster contain approximately the same number of profile measuring points (approximately 90 points each), which varies the cluster extent between 0.1 m and 4 m.

In addition, a B-spline approximation is superimposed on the measuring points in black. For the theoretical background see e.g. [10], [11] or [3].

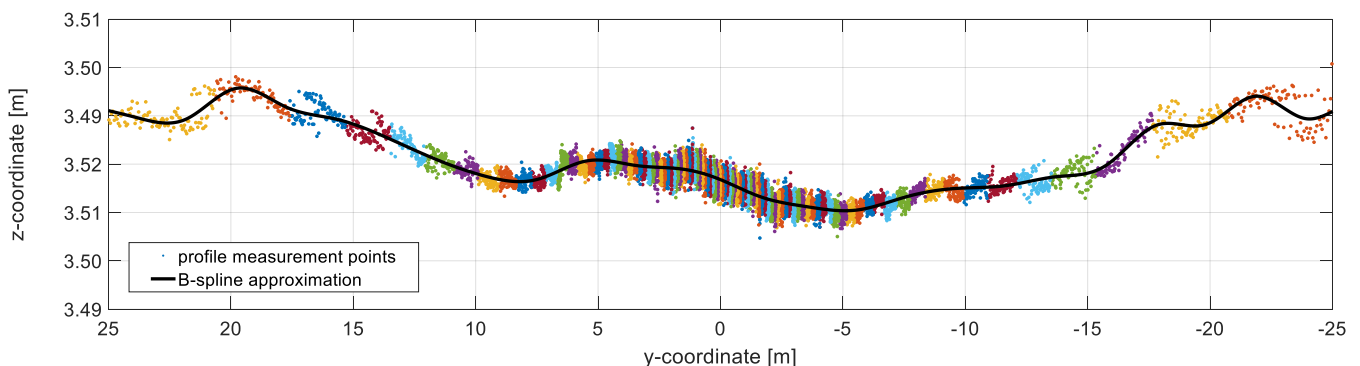


Fig. 12 Results of two processing methods: spatial clustering (colored) and B-spline approximation (black).

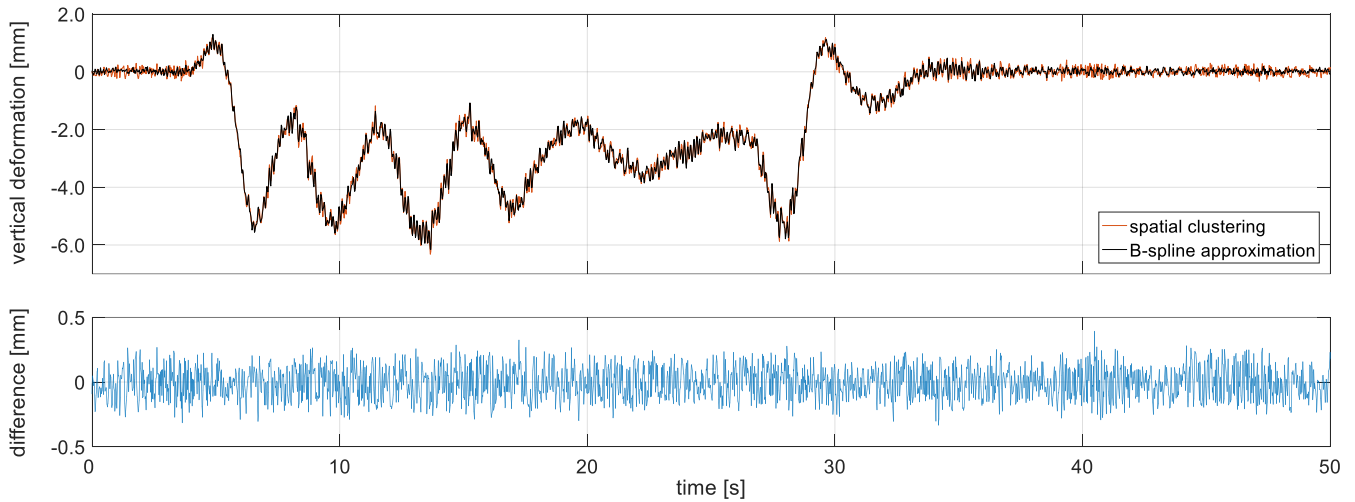


Fig. 13 Time series of the z-coordinates of both processing methods at the y-coordinate -10.39 m and their differences.

In order to compare the results of the two profile-wise spatial processing methods, the same positions on the supporting structure were evaluated. These positions are specified in this case by the representatives of the 100 clusters and were also evaluated with the B-spline approximation. Therefore a total number of 100 time series distributed over the entire structure are available.

In the upper diagram in Figure 13, the time series of the z-coordinates for both processing methods are shown exemplary for one position on the structural member (y-coordinate -10.39 m). It is a 50-second section of the crossing of a freight train, which was recorded with 50 Hz and contains therefore 2.500 measurements.

The lower diagram shows the differences between those two processing methods. Those differences do not contain any systematic effects and are mainly caused by the slightly larger noise level of the spatial clustering. This is why we only look at the results of the profile-wise B-spline approximation in the following.

The time series in the upper diagram of Figure 13 consists primarily of a low-frequency signal component due to the load of the train and a superpositioned high-frequency signal component due to the dynamic excitation of the bogies of the train. In the following, these two parts are called the quasi-static and the dynamic signal component of the time series.

With the use of the multiresolution analysis (MRA) of the discrete wavelet transform for the time series not only noise can be eliminated, but it is also possible to separate frequency ranges. The MRA to be used decomposes the signal into individual frequency bands, see e. g. [12] or [13]. With the wavelet synthesis the wanted signal components can be reconstructed and thus, the transition from the total deformation to the dynamic signal component can be realized, see Figure 14.

In the upper diagram, the black line shows the quasi-static signal component determined by means of wavelet decomposition/synthesis. The time series of the dynamic deformation component is shown in blue in the lower diagram.

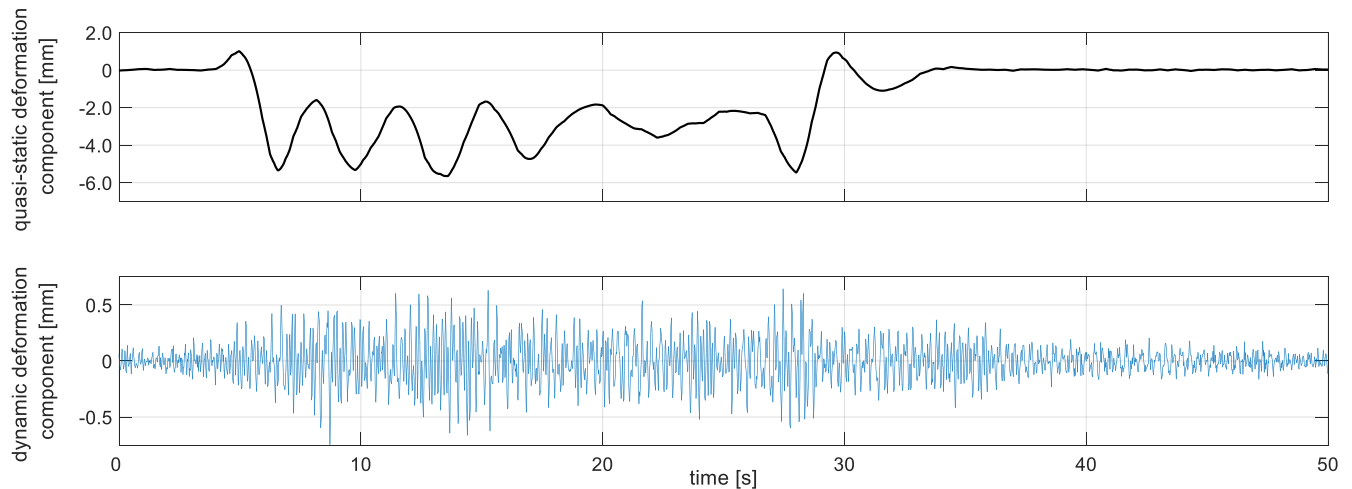


Fig. 14 Separation of the dynamic and quasi-static deformation component of the sample time series from Figure 13.

Based on the separation of the quasi-static from the dynamic deformation component, two selected positions on the structural member are analyzed in the following. These are a position in the middle of the field (y-coordinate: -0.0 m, yellow) and approximately the quarter point (y-coordinate: -10.39 m, purple). These two positions are highlighted in the top chart in Figure 15 with colored dots and also in Figure 16 with colored lines. The choice of these positions is based on the theoretical eigenmodes of a simple beam [14], shown in Figure 16. This simple model can also be a good approximation for simple bridges.

While in the middle of the beam the first eigenmode has its maximum, the second eigenmode has a zero pass. In the quarter point, however, the second eigenmode has its maximum, while the amplitude of the first eigenmode decreases.

In the diagrams shown below in Figure 15, the dynamic deformation components in the time series of the individual positions are shown on the left side and the corresponding amplitude spectra on the right side. For the two positions on the structure, three ranges can be identified in the amplitude spectra, in which frequencies occur above the noise level: approximately at 2-3 Hz, at 5 Hz and at 8 Hz.

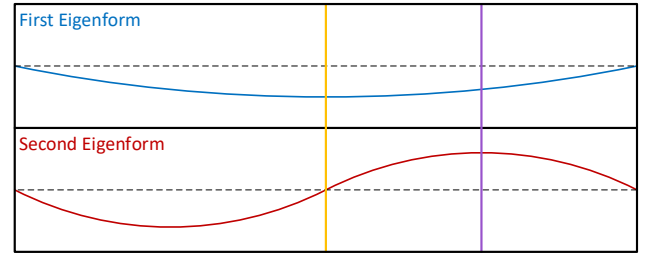


Fig. 16 Theoretical eigenmodes of a beam.

The so far considered time series underlying the amplitude spectra include the train crossing, as well as areas in which the supporting structure is at rest and also the free decay process of the structure. Therefore it is not possible to make a valid statement about the association of those frequency ranges to the natural frequencies. In principle, you can only see that certain frequencies within the time series have occurred at least temporarily.

To avoid this problem we will concentrate on a shorter part of the time series: the free decay process after the train left the monitored bridge span. Due to the high spatial resolution of the profile scanner we can simultaneously widen our view in the context of spatial resolution.

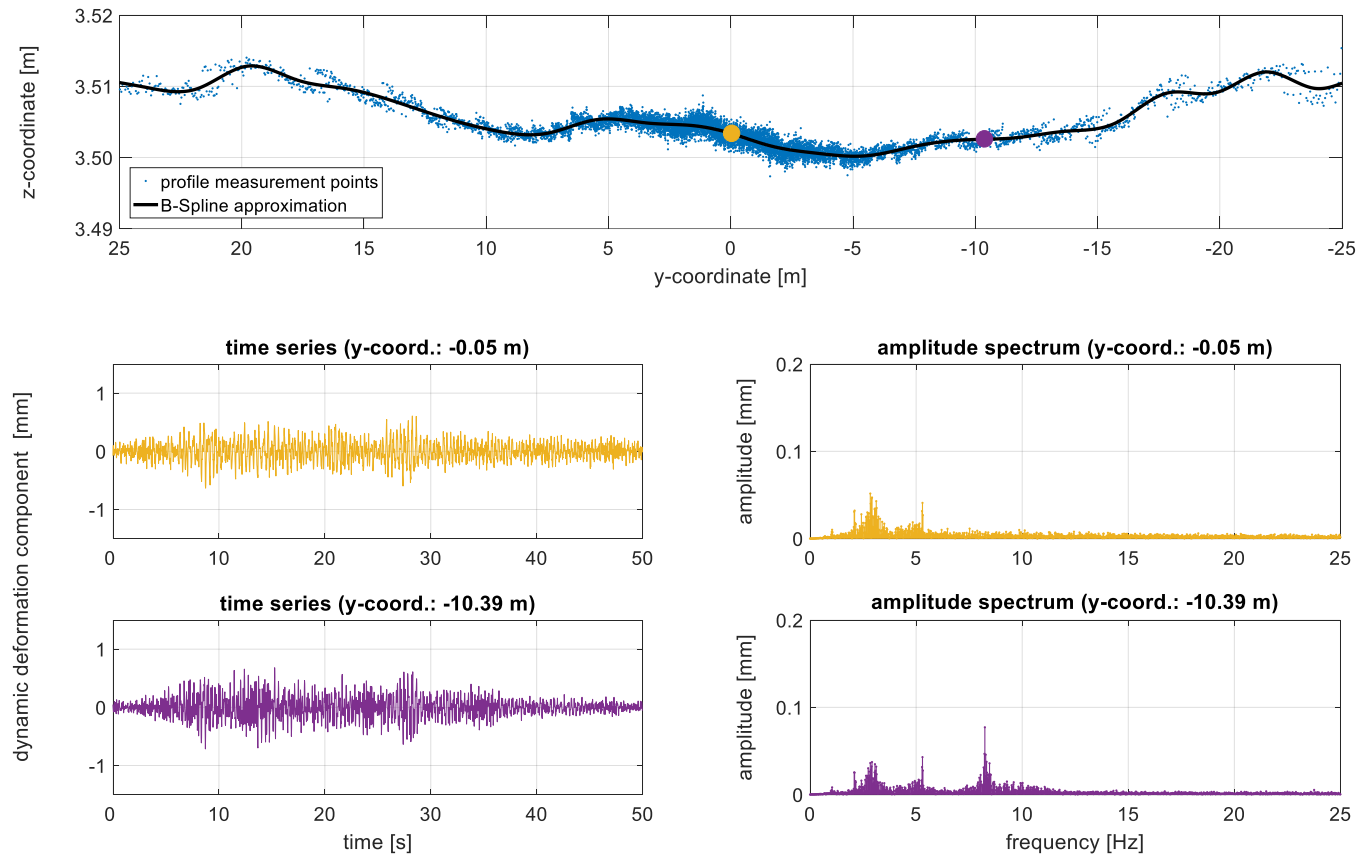


Fig. 15 Dynamic deformation component in the time- and frequency domain at two discrete points of the bridge span.

The two position representation in Figure 15 corresponds to the traditional analysis of classical sensors used for the monitoring of bridges. However, the almost space-continuous detection of the structural surface with the profile scanner can be used to view the entire bridge span in detail, maintaining a temporal resolution of 20 ms, for a corresponding waterfall representation see Figure 17.

On the x-axis the position on the structure is shown, on the y-axis the frequency range (limited to the relevant area up to 12 Hz) and on the z-axis the magnitude of the amplitudes is plotted.

Thus, the free decay process is represented in the frequency domain for the entire bridge span.

In Figure 17 significant amplitudes occur only at the frequencies of 3.1 and 8.3 Hz. The previously occurring amplitudes at 5 Hz and the secondary maxima in the frequency range around 3 Hz are, however, no longer existing, compared with Figure 15.

Hence, it can be concluded that 3.1 Hz is the first natural frequency (eigenfrequency) and 8.3 Hz is the second natural frequency. Since the associated distribution of the amplitude maxima corresponds mostly to the theory as seen in Figure 16.

This is further confirmed by the phase position of the occurring frequencies, which is constant for 3.1 Hz (first natural frequency) over the entire structure, while the phase position for 8.3 Hz (second natural frequency) is symmetrically to the middle of the bridge, but with inverse sign.

However the amplitudes of the likely second eigenmode increase on both sides till the end of the measured bridge span. According to the theory from Figure 15 there should be a decrease in amplitude beginning at the quarter point till the support. This difference between the theory and the profile scanner measurements is likely caused by the too simple model, which does not take the real support conditions and the fact that the bridge consists of seven bridge spans into account.

Those differences can only be evaluated with the high spatial resolution of the profile scanner. Otherwise only measurements at predefined points are carried out in most cases according to the theory, like the graphs depicted in Figure 15.

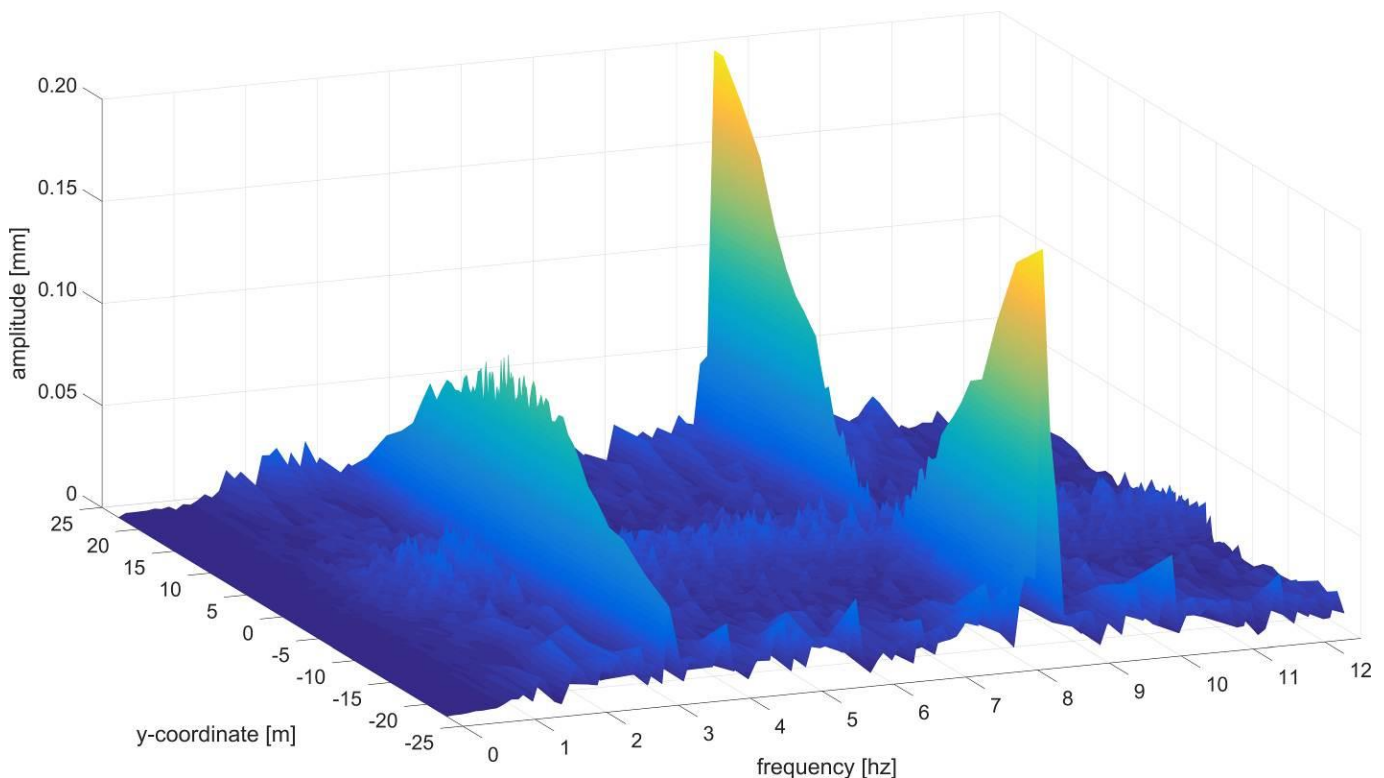


Fig. 17 Amplitude spectra of the dynamic deformation component for the free decay process of the monitored bridge span.

6. Conclusions

Those two examples demonstrate that a non-contact measuring system like a profile scanner can capture temporally variable structural deformations more efficiently and in a much higher spatial resolution than typically used sensors for the monitoring of supporting structures. Furthermore it is possible, with the presented measurement and evaluation methodology, to reach uncertainties of nearly the same scale as generated with classical discrete measurement sensors.

Due to the high spatial and temporal resolution large amounts of data are recorded. For practical use, this implies that the automatically collected data needs a largely automated processing and quality assessment.

With the spatio temporal processed data basis it is possible to derive deformation measurements at nearly any desired position within a supporting structure profile (post mission). Therefore the dependence on prior knowledge about the structure or on the theoretical deformation behavior is greatly reduced. That applies to the measurement planning as well as the analysis of the deformation behavior.

The adaptable spatial resolution furthermore enables the detection of model disruptions or deviant behavior of parts of the supporting structure. Thus, it is possible to verify structure models and to improve their predictive quality accordingly.

References

- [1] Otto Heunecke, Heiner Kuhlmann, Walter Welsch, Andreas Eichhorn and Hans Neuner, Handbuch Ingenieurgeodäsie - Auswertung geodätischer Überwachungsmessungen, Springer-Verlag, ISBN: 9783879074679, 2013
- [2] Zoller + Fröhlich, Z+F PROFILER® 9012 Datasheet, URL: http://www.zf-laser.com/fileadmin/editor/Datenblaetter/Z_F_PROFILER_9012_Datenblatt_D_final_kompr.pdf (visited at 20. 07. 2018), 2018
- [3] Florian Schill, Überwachung von Tragwerken mit Profilsclannern, Dissertation, Technische Universität Darmstadt, Darmstadt, 2018
- [4] Florian Schill and Andreas Eichhorn, Automatische Segmentierung von Profilsclannermessungen am Beispiel von Brückenbauwerken, Ingenieurvermessung 17, Beiträge zum 18. Internationalen Ingenieurvermessungskurs Graz, Graz, 2017
- [5] Carl De Boor. A practical guide to splines. Applied mathematical sciences, Springer-Verlag, ISBN: 9780387953663, 2001
- [6] David L. Donoho and Iain M. Johnstone, Ideal spatial adaptation by wavelet shrinkage, Biometrika 81.3, S. 425–455, 1994
- [7] Florian Schill and Andreas Eichhorn, Investigations of low- and high-frequency movements of wind power plants using a profile laser scanner, 3rd Joint International Symposium on Deformation Monitoring (JISDM), Vienna, 2016
- [8] Jia Liu, Einfluss der Schienenbefestigungskomponenten auf das laterale Verformungs- und Lastverteilungsverhalten der Schiene, Dissertation, Technische Universität München, München, 2011
- [9] Matthias Becker, Birgit Traiser, Florian Schill, Jens Schneider and Andrei Firus, Messung und Identifikation dynamischer Strukturparameter mittels terrestrischer Mikrowelleninterferometrie, Messen im Bauwesen, 2016
- [10] Hans Neuner, Claudius Schmitt and Ingo Neumann, Modelling of terrestrial laser-scanning profile measurements with B-Splines, Proceedings of the 2nd Joint international Symposium on Deformation Monitoring (JISDM), Nottingham, 2013.
- [11] Johannes Bureick, Hamza Alkhatib and Ingo Neumann, Robust Spatial Approximation of Laser Scanner Point Clouds by Means of Free-form Curve Approaches in Deformation Analysis, Journal of Applied Geodesy 10.1, S. 27–35, 2016
- [12] Werner Bäni, Wavelets: Eine Einführung für Ingenieure, Oldenbourg Verlag, ISBN: 9783486594003, 2005
- [13] Donald B. Percival and Andrew T. Walden, Wavelet Methods for Time Series Analysis, Cambridge Series in Statistical and Probabilistic Mathematics. Cambridge University Press, ISBN: 9780521640688, 2000
- [14] Dietmar Gross, Werner Hauger and Peter Wriggers, Technische Mechanik 4: Hydromechanik, Elemente der Höheren Mechanik, Numerische Methoden Springer-Verlag, ISBN: 9783662556948, 2018

Position Determination of a Moving Reflector in Real Time by Robotic Total Station Angle Measurements

Gabriel Kerekes, Volker Schwieger

Received: September 2018 / Accepted: October 2018 / Published: December 2018
© Journal of Geodesy, Cartography and Cadastre/ UGR

Abstract

Angle readings from Robotic Total Stations (RTS) can be acquired with a very high update rate in comparison with the update rate of the distance measurement. For short ranges these readings can be considered more accurate than the distance measurements. The currently presented system makes use of this feature and combines measurements captured from two Leica high precision RTS that have Automatic Target Recognition (ATR) sensors in order to determine the position of a moving reflector in real time based solely on angles. Both RTS are stationed in the same coordinate reference frame and controlled by a central computer running a LabVIEW program. It retrieves the angle measurements and calculates the current position of the moving reflector based on angle intersection principles. This increases the positioning frequency of the RTS system to 20 points/second, which is twice as fast as the normal tracking mode of these specific RTS. A miniature railway and trolley are used to move the studied reflectors.

In the first tests, different positions of reflectors placed on a stationary trolley are determined and compared to positions coming from classical measurements of angles and distances. The differences are in this case less than 1 mm. Further experiments, present the achieved position in kinematic mode by means of lateral deviations to a reference line, leading to an average value of 2.1 mm for the 360° reflectors and 3.3 mm for a normal reflector.

Keywords

Automatic Target Recognition, angle intersection, real time positioning.

1. Introduction

Angle measurements can be considered the oldest means of determining the position of a remote object. These are used for purposes that vary from determining geodetic networks to close range photogrammetry.

The principle of angle intersections is nowadays mostly utilized in Theodolite Measurement Systems (TMS) that imply simultaneous measurements from at least two theodolites. After establishing a common coordinate reference system, the measured angles are used to calculate the 2D or 3D position of the desired objects. Depending on the distance between the theodolites and the angle measurement accuracy, very high accuracies are achievable. For example, with a base length of 10 m and angle measurement standard deviation of 0.7 mgon, objects up to 10 m can be determined with a precision of 0.3 mm (Hennecke et al., 1992). This is possible for nonmoving objects only. In order to extend the functionality of such a system to a kinematic application, the theodolites must be capable of following the moving object and delivering the raw data for processing in real time. Even though the idea is not new, there are, to our concern, few or tangential publications on this topic.

A RTS has a tracking function that can be used in combination with a reflector to reach the aforementioned purposes. For short ranges, accuracy of the point position is mostly influenced by the distance measurement. In comparison with the distance measurement, angle readings are available with a much higher update rate. In real time kinematic applications that rely on a RTS for positioning, 3D coordinates are determined using angle and distance measurements. This fact limits the position update rate to the distance measurement update rate.

In this paper, two Leica high precision RTS (TS 30 and TS16i) that are equipped with Automatic Target Recognition (ATR) sensors are used to deliver angle measurements to an external computer that calculates the position of a moving reflector in real time based solely on angles. The functional model and hardware implementation are explained in detail in the second part of the article.

Experiments undertaken in laboratory conditions, present the

M. Sc. Gabriel Kerekes, Prof. Dr.-Ing. habil. Volker Schwieger
Institute of Engineering Geodesy, University of Stuttgart
Geschwister-Scholl-Str. 24D, 70174 Stuttgart, Germany
gabriel.kerekes@iigs.uni-stuttgart.de
volker.schwieger@iigs.uni-stuttgart.de

achieved position of several reflectors placed on a moving trolley running on a miniature railway. This simulates a kinematic application that can resemble guidance and control processes for construction machines. The results are afterwards compared with measurements taken in static mode and tracking mode. Further enhancements and examples of possible applications are given in the last part of the paper.

2. Functional model and hardware implementation

Starting with the middle 80' electronic TMS became popular on the market as a solution to the high precision demands of industrial measurements. In Bill (1985) information about the functioning principles and first available hardware and software solutions from the companies Keuffel & Esser (Breithaupt), Kern, Zeiss and Wild has been published. In the same publication, examples of applications have been given and it can be commonly accepted that since then, the components of a TMS have seen many enhancements, but the principles remained basically the same.

The currently presented system resembles a TMS, but certain steps of the measurement and computation process are done differently. Figure 1 represents the setup with its individual components and computed or measured values needed for calculating the position of the moving target. In a first phase, RTS 1 will play the role of the system origin, thus fictionally receiving the coordinates $(0,0,0)$ and the RTS 2 receives $(0,b,\Delta z)$.

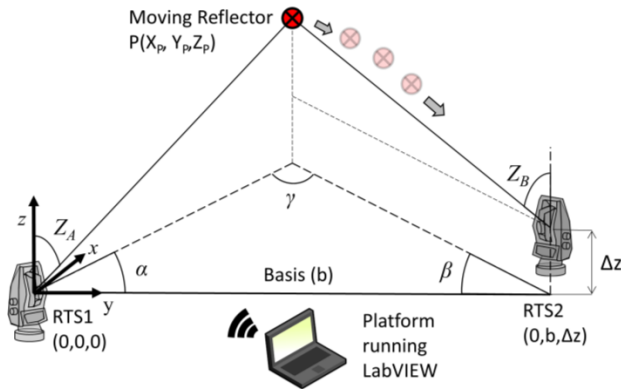


Fig. 1 – System components and measured/computed values

Intersection approach measures angular (direction) observations to the unknown position; with the measuring instrument occupying each of the known stations. It has the advantage of being able to position an unknown point which cannot be physically occupied (Awange et al., 2010). Nevertheless, in the presented system, the observed object needs to be accessible at least once when fixing the reflector. Afterwards, the only condition is that the line-of-sight between each RTS and the reflector is not interrupted during the measuring process.

Before the actual measurement, there are some steps that need to be followed. The 3D coordinates for both RTS need to be determined in a local or global coordinate system. There are multiple methods of doing this, but here a predefined known coordinate frame has been used to determine the station points through resection (Möser et al., 2012). Besides the position of the RTS, the orientation of the coordinate system is fixed, too. From this point on, several elements can be calculated. The 2D distance b is determined as the Euclidian plane distance between the two RTS and the height difference Δz by subtracting the two heights. Also the orientation angle t_{12} between the origin RTS and the second RTS is calculated with help of coordinates.

The next step implies calculating the plane angles α and β with the help of the orientation angle in each point of time as follows:

$$\alpha = t_{12} - r_{1P} \quad \beta = \pi - t_{12} + r_{2P}$$

where r_{1P} and r_{2P} are the directly measured directions from the RTS to the observed point P.

Having these, the relative coordinates may be delivered by the following equations (Kahmen, 2006):

$$\Delta x = b \cdot \frac{\sin \alpha \cdot \sin \beta}{\sin(\alpha + \beta)} \quad \Delta y = b \cdot \frac{\cos \alpha \cdot \sin \beta}{\sin(\alpha + \beta)}$$

$$\Delta z = \frac{1}{2} \cdot \left(b \cdot \frac{\sin \beta \cdot \cot Z_A + \sin \alpha \cdot \cot Z_B}{\sin(\alpha + \beta)} + \Delta z_{AB} \right)$$

These relative coordinates are available in a Cartesian Coordinate System (CCS) in which the origin is fixed in the optical center of one RTS, the y-axis is pointing horizontally the second RTS, the x-axis is perpendicular on the y-axis and the z-axis corresponds with the plumb line of the first instruments. Due to this fact, absolute coordinates of the observed point are retrieved only after a transformation. One simple method implies transforming the plane coordinates with the aid of the rotation angle between CCS and the absolute or local coordinate system in which the RTS were stationed as follows:

$$\begin{aligned} \varphi &= t_{12} - \frac{\pi}{2} \\ X_P &= X_O + \Delta x \cdot \cos \varphi - \Delta y \cdot \sin \varphi \\ Y_P &= Y_O + \Delta x \cdot \sin \varphi + \Delta y \cdot \cos \varphi \\ Z_P &= Z_O + \Delta z \end{aligned}$$

All these equations yield the functional model that is implemented in the LabVIEW graphical programming interface. Some input parameters like the coordinates of the RTS and implicitly basis length and orientation do not change during the measuring process. These are considered error free, even though this is not entirely true even in laboratory conditions. Other elements like the directions and zenith angles are constantly changing during the measurement process. In order to accomplish these tasks, the two RTS are connected via a serial connection RS232 to the computer running LabVIEW. A constant inquiry about the current status of the RTS takes place and as a response, the

two angles are retrieved. In comparison with other connections, the serial one is preferred due to its standardization and simplicity of use (Georgi & Metin, 2007). This is also facilitated from the RTS manufacturer's side through the Leica GeoCOM interface which permits server-client based interactions (Leica Geosystems, 2018). The GeoCOM command used for the angle measurement is TMC_GetAngle5. If more information about each angle measurement is needed, the command TMC_GetAngle1 can be used to obtain internal or instrument specific information, but for the present case most of that information is redundant.

None of the above described implementations would have made sense if the ATR Module in the RTS had not tracked the reflector with a high frequency of about 20 Hz. This has also been tested and proved in Lienhart et al. (2017). Shortly described, a laser beam is emitted and based on the projected laser spot that returns from a reflector on the CMOS-Picture-Sensor, the difference between the reflector center and crosshair center can be calculated and reduced to 0 by guiding the telescope. Considering that the processing in the ATR module takes place with a speed of up to 200 picture segmentations per second, following a reflector is a stable process even at short ranges (Stempfhuber & Kirschner, 2008). The Leica TS30 has an ATR Module and the Leica TS16 benefits from the enhancements of the ATRPlus Module. For more specific technical information about these developments, the reader should consult Stempfhuber & Kirschner (2008), Grimm et al. (2015) and Kleemaier et al. (2016).

Another decisive factor worth mentioning is the reflector. Usually, 360° reflectors are used in tracking applications due to the flexibility offered by the angle of incidence between line-of-sight and reflector. Nevertheless, due to the constructive solution of these reflectors, mostly made out of six bundled single prisms, there are several negative influences on the measurements of horizontal respectively vertical angle and slope distance. These lead to, depending mostly on how the 360° reflector is rotated, systematic position falsification of up to 8 mm; a fact proved in Lackner & Lienhart (2016). It is mostly due to double reflections at close ranges of the same reflector on the CMOS-Picture-Sensor; in this case the telescope may be directed to the "false" reflector center. A solution to overcome this issue is to use a normal reflector which is not subject to such systematic errors, but the disadvantage is, that the maximum incidence angle at which ATR still functions is around 50gon. If only one RTS is needed in the tracking application, there are some possible solutions of using a normal reflector and adapting it to a sensor platform that actively turns to always face the observing instrument (Horst & von Gösseln, 2012). Normally such enhancements are used for active targets working in combination with laser trackers.

After having the hardware and software components set up, several experimental measurements were made to firstly test the system and secondly have an idea about the offered accuracy based on comparisons between the different measurement modes.

3. Experiments

Three different Leica reflectors were put to test in two measurement setups (figure 3). The main difference between them is the position of the two RTS with respect to the reflectors. In case 1, a normal reflector cannot be adequately tested due to the increasing angle of incidence when the reflector is approaching the base. After a certain point, the ATR Module cannot track the reflector anymore; therefore, case 2 is studied to evaluate the system with a normal reflector. In case 1 the base (b) has around 4 m and case 2 it is reduced to 1.5 m. The distances to the moving reflectors vary in both cases from 1 m to 3 m.

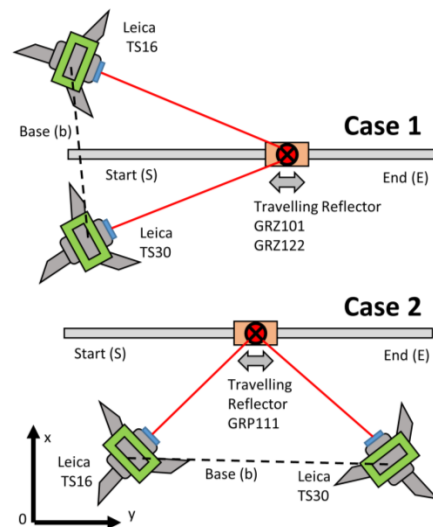


Fig. 3 – Measurement setups used to test the functionality of the system

In each case, the reflectors were mounted on a trolley (figure 4) that can be manually shifted on a miniature railway in two directions. This was chosen mainly for two reasons:

- ease of testing and repeatability
- resemblance to mobile measurement systems that rely on total station assisted measurements e.g. (Amberg Technologies, 2018).



Fig. 4 – Miniature trolley with the used reflectors (from left to right: Leica Miniprisma GMP111, Leica 360° Miniprisma GRZ101, Leica 360° Prisma GRZ122)

After the resection has been completed for both RTS, the coordinates of the station points can be introduced or uploaded; the user must manually aim the target once and the connection can be started. From this point on, based on the calculated and measured values, the program delivers the position of the reflector with an update rate of 20 Hz. After terminating the program, the user can save the data for further analysis.

3.1 Static test

To verify the calculated coordinates, several points were measured while the trolley was stationary. These values were compared to the position obtained from a normal measurement (angles and distances) from each RTS. As it can be seen in table 1, the differences are very small, all of them having a magnitude of less than 1 mm. Even though a functional relationship between the intersection angle γ and these differences was expected, this test has yielded inconclusive results. The theoretical aspects for an optimal configuration regarding basis, angle and distance to the observed objects can be read in Kersting (1987).

Table 1 Differences between polar measured positions on the miniature railway and angle determined positions in static mode

Point	dX (mm)	dY (mm)	dZ (mm)	Intersection Angle(γ) (gon)
GRZ101-1	0.03	-0.75	0.08	93
GRZ101-2	0.25	-0.95	0.34	110
GRZ101-3	0.70	-0.75	0.40	133
GRZ101-4	-0.55	-0.45	0.35	165
GRZ122-1	-0.25	0.40	0.30	93
GRZ122-2	-0.85	-0.35	0.30	110
GRZ122-3	-0.33	-0.83	0.20	132
GRZ122-4	-0.18	-0.50	0.32	165
GMP111-1	0.35	0.10	0.00	29
GMP111-2	-0.40	-0.07	0.01	31
GMP111-3	-0.95	0.17	0.15	31
GMP111-4	-0.39	0.20	-0.03	28

The errors are well below a mm for all coordinates components; mainly they are on a tenth-mm level. Consequently, it can be assumed that the functional model leads to reliable positioning for static reflectors.

3.2 Kinematic test

For the kinematic tests, a reference was defined as measure of comparison. This reference is a straight line that best fits several points measured along the miniature railway in a stable state of the trolley. In such applications, lateral deviations are a good indicator for the achieved positioning quality. Therefore, each single point measured during the trolley movement is projected onto the reference line and the resulting distance is colored depending on its

magnitude. Figure 5 represents the lateral deviations with regard to the reference line for each reflector.

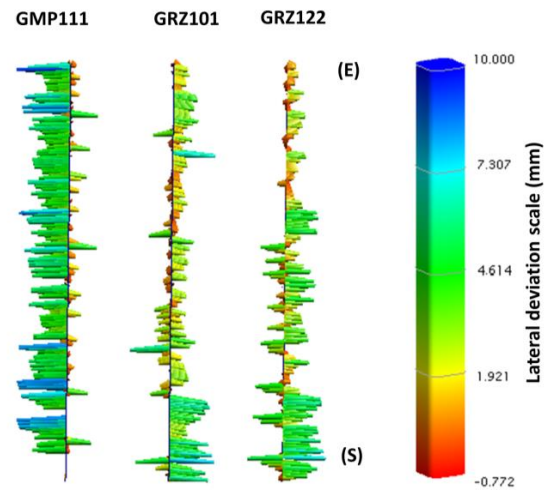


Fig. 5 – Lateral deviations with the position obtained in real time via angle measurements only (magnified 25x)

After the first tests, a systematic effect on the lateral deviations has been observed. The determined positions were all directed towards the TS30. This led to the conclusion that the two RTS are not delivering data simultaneously, therefore synchronization of the data transfer rate needs to be achieved. Unlike in Schwieger et al. (2010) where the position of a point is influenced by internally (RTS) synchronized angles and distances, here the synchronization problem is extended to the whole system comprised of the RTS.

Analyzing the data of both RTS, a time delay of 50 ms for all TS30 angles was empirically derived and afterwards applied in the software. This leads to an average lateral deviation in case 1 of 2.1 mm with the maximum deviation of 7 mm. In case 2 using the reflector GMP111 led to an average lateral deviation of 3.3 mm. Simulations show that lateral deviations based on the angular measurement accuracy in this case should be smaller than 1 mm, but this was not reached. Even after applying the time offset correction, the majority of the positions in case 2 were directed towards the instruments. Because reflector has a limited aperture angle ($\sim 30^\circ$), the RTS showed difficulties of following it after a certain position.

During the tracking process angles are continuously used for position determination, but if one of the RTS receives a doubtful reflection (e.g. another reflector in the background) it shortly searches for the reflector again, fact that falsifies the position for short moments of time. Even if the search window is very narrow, the movements opposite to the travelling direction lead to outliers.

An independent test has been performed for the two cases, with one RTS set in synchro-tracking mode. This is what normally occurs when a single RTS is used for guidance and control. The single points are then obtained as polar points. Only the positions from one RTS in tracking mode (Leica TS30) are represented in the same way as before (figure 6).

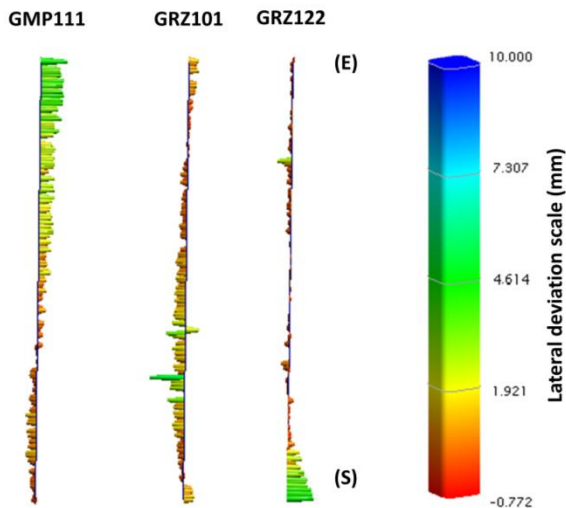


Fig. 6 – Lateral deviations with the position obtained in synchro-tracking mode via angle and distance measurements (magnified 25x)

A first observation is that all the lateral deviations of the points obtained in the tracking mode are smaller for all reflectors. The mean value of the lateral deviation for both 360° reflectors is 1.3 mm and for the miniprism 2.0 mm. In these specific conditions, the results are better than the ones obtained with the angles only measurements. A disadvantage is that the maximum measurement frequency is 10 Hz, but after analyzing the data, an average of only 6 Hz was reached in reality. Currently, high-end RTS that reach a maximum measurement frequency of 20 Hz are available on the market, but the present study dealt only with the presented RTS.

4. Conclusions

One of the main goals of this work was to present a possibility of increased position determination rate with the aid of angle measurements only received from a network of RTS (Kerekes & Schwieger, 2018). A LabVIEW program has been developed to connect the two RTS and based on principles of TMS, to deliver the position of a moving reflector with an update rate of 20 points/second. This is the current state of the developed system and further improvements are under research.

The synchronization issues that were encountered are not entirely resolved because there are many sources that affect the data flow. Solutions presented by Thalmann & Neuner (2018) in which Network Time Protocol is used to synchronize sensors may be adopted to determine the time offset and drift if these are present. Another possible improvement is a data filter that would automatically eliminate positions during the searching phase, therefore eliminating biased positions of the reflector.

A system that presents one order of higher accuracy degree can be used to establish a reference and help at calibrating the system. Lerke & Schwieger (2015) used measurements

from a laser tracker as reference values to determine possible systematic errors and evaluate the positioning quality.

Nevertheless, if the desired accuracy is within the current limits (under 5 mm), the system can serve as a positioning sensor for kinematic application or guidance and control of machines, unmanned aerial vehicles or robots that are depending on a high position update frequency. In the context of building fast and efficiently, such systems may be used in combination with fast moving construction machines that benefit from a high positioning update rate. This generally reduces the control process.

All in all, advantages of the presented RTS System are flexibility, good positioning quality and high update rate of up to 20 Hz while facilitating the use with little or no user interference.

References

- Amberg Technologies AG, Amberg Survey GRP100 Brochure, retrieved from www.amberg.ch, last accessed on 09.2018
- Awange J.L., Grafarend E.W., Paláncz B., Zaletnyik P., Positioning by intersection methods, Algebraic Geodesy and Geoinformatics, p. 249, ISBN 978-3-642-12123-4, Berlin Heidelberg, 2010
- Bill, R., Automatische Meß- und Berechnungssysteme für den Industriebereich, Allgemeine Vermessungs-Nachrichten, Heft 6, p. 205-210, Karlsruhe, 1985
- Georgi, W., Metin, E.: Einführung in LabVIEW, p. 279, 3. Auflage. ISBN 978-3-446-41109-8, Munich, 2007
- Grimm, D., Klemaier, G., Zogg, H-M.: ATR Plus Whitepaper. Leica Geosystems AG, retrieved from www.myworld.leica-geosystems.com, last accessed on 09.2018, published 2015
- Hennecke, F., Müller, G., Werner, H., Handbuch Ingenieurvermessung, Band 6, Maschinen- und Anlagebau, p. 85, ISBN 3-87907-242-6, Karlsruhe, 1992
- Horst, S., von Gösseln, I., Active Prism for Total Station Measurements, Proceedings of Machine Control & Guidance, ISBN 978-300-037295-7, Stuttgart, 2012
- Kahmen, H., Angewandte Geodäsie Vermessungskunde, p. 297, 20. Auflage, ISBN 978-3-11-018464-8, Berlin, 2006
- Kerekes, G., Schwieger, V., Kinematic Positioning in a Real Time Robotic Total Station Network System, proceedings of 6th International Conference on Machine Control & Guidance, Berlin, 2018
- Kersting, N., Optimale Konfiguration beim Vorwärtseinschneiden mit Industriemeß-Systemen, Allgemeine Vermessungs-Nachrichten, Heft 5, p. 169-178, Karlsruhe, 1987

Kleemaier, G., Maar, H., Zogg, H-M.: Enhanced automation performance of Total Stations for kinematic applications using the ATRplus technology, proceedings of 5th International Conference on Machine Control & Guidance, Vichy, 2016

Lackner, S., Lienhart, W.: Impact of Prism Type and Prism Orientation on the Accuracy of Automated Total Station Measurements, Proceedings on Joint International Symposium on Deformation Monitoring, Vienna, Austria, 2016

Leica Geosystem AG, The GeoCOM Reference Manual, retrieved from www.myworld.leica-geosystems.com, last accessed on 09.2018

Lerke, O., Schwieger, V., Evaluierung der Regelgüte für tachymetrisch gesteuerte Fahrzeuge, ZFV, Heft 4, p. 211-221, ISSN 0044-3689, Augsburg, 2015

Lienhart, W., Erhart, M., Grick, M., High frequent total station measurements for the monitoring of bridge vibrations, Journal of Applied Geodesy, Vol. 11/1, ISSN 1862-9016, Berlin Boston, 2017

Möser, M., Hoffmeister, H., Müller, G., Staiger, R., Schlemmer, H., Wanninger, L., Handbuch Ingenieurgeodäsie: Grundlagen, p. 387, ISBN 978-3-87907-504-1, Berlin, 2012

Schwieger, V., Beetz, A., Wengert, M., Schweitzer, J.: Echtzeit-Integration ingenieurgeodätischer Messsysteme in Bauregelkreise 16. Internationaler Ingenieurvermessungskurs, p. 45-47, ISBN 978-3879074921 Munich, Germany 2010

Stempfhuber, W., Kirschner, H., Kinematische Leistungsfähigkeit von zielverfolgenden Tachymetern – Ein Beitrag zum Stand der Technik am Beispiel des Leica TPS1200+, Allgemeine Vermessungs-Nachrichten, Heft 6, p. 216, ISSN 002-5968, Heidelberg, 2008

Thalmann, T., Neuner, H., Untersuchung des Network Time Protocols für die Synchronisation von Multi-Sensor-Systemen, Allgemeine Vermessungs-Nachrichten, Heft 6, p. 163, ISSN 002-5968, Berlin, 2018

Aspects of Intra-Frame Velocity (Deformation) Models for the United States National Spatial Reference System in 2022

Daniel Roman¹

Received: September 2018 / Accepted: October 2018 / Published: December 2018
© Journal of Geodesy, Cartography and Cadastre/ UGR

Abstract

The National Oceanic and Atmospheric Administration's (NOAA) National Geodetic Survey (NGS) will be updating the National Spatial Reference System (NSRS) for the United States in 2022. Four Terrestrial Reference Frames (TRF's) will be defined based on the available ITRF in 2020. Euler Pole Parameters (EPP) will be determined for each frame to capture most of the horizontal plate motion. An Intra-Frame Velocity Model (IFVM) is required to account for any residual horizontal and all vertical motion within these frames. These are essentially deformation models but can be extended across the plate boundaries for practical purposes. Hence, the use of Intra-Frame instead of Intra-Plate. This paper will cover significant aspects of the IFVM that rely on increasingly sophisticated (and complicated) techniques for capturing the motion within each TRF. Simply gridding the National CORS network is the easiest and least accurate approach. The most complicated and potentially most accurate would be the use of InSAR. NGS must select the most cost-effective and accurate mechanism within the next few years to have the IFVM in place by 2022.

Keywords

Capacity building; Positioning; Reference Frames; Reference Systems; Cadastre

1. Introduction

NOAA's National Geodetic Survey (NGS) is responsible for defining, maintaining and providing access to the National Spatial Reference System (NSRS) that is the U.S. SDI. NGS will update the NSRS in 2022 to align more closely with International Terrestrial Reference Frame existing at that time. The most recent realization is ITRF 2014 [1], and this may still be in use in 2022 [pers. comm. Altamimi 2018].

The NSRS in 2022 will consist of Terrestrial Reference Frames (TRF) covering all U.S. States and territories on four plates: North America, Caribbean, Pacific and Mariana. These four TRF's will be the same as ITRF2015 at epoch 2020.0 but then diverge based on plate rotations and deformation models.

This paper provides a general overview with an emphasis on deformation models that will describe the expected motion in each of the four frames. Further background is available in the NGS Blueprint Part 1, Blueprint Part 2, and New Datums webpage [6,7,8].

2. National Spatial Reference System (NSRS) in 2022

The NGS Blueprint Part 1 [6] serves as the primary reference for this update.

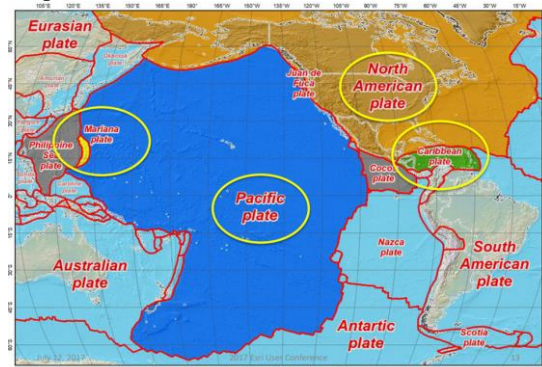


Fig. 1 The four tectonic plates "fixed" for the 2022 terrestrial reference frame.

¹ Aspects of IFVM for the US NSRS in 2022 D. Roman
U.S. Department of Commerce, NOAA's National Geodetic Survey
1315 East-West Highway
SSMC3, N/NGS
Silver Spring MD 20910 USA
E-mail: dan.roman@noaa.gov

a. Four Frames Tied to an ITRF Model

The basic concept is that of a densified ITRF model with Euler pole transformations defined for each of the plates circled in Figure 1: North America, Caribbean, Pacific, and Mariana.

At a definitional epoch, the four frames above (NATRF, CATRF, PATRF, & MATRF, respectively) would be identical to the reference ITRF model, presumably ITRF 2014. The likely epoch would be 2020.0. Before and after that date, the four frames would rotate specific to their own Euler pole parameters that will be determined from a select set of Continuously Operating Reference Stations (CORS) on each plate.

b. Foundation CORS (FCORS)

Most CORS represent voluntary contributions from outside groups. NGS makes data available from nearly 2000 such sites on its website. NGS is responsible for managing and archiving the data, but has little authority to actually maintain and upgrade such sites. NGS actually operates only about 40 stations, which are actually focused on missions other than that for NGS.

As such, NGS will be divesting itself of these other sites with the intent to develop NGS-owned sites that will serve as fiducial control sites of the NSRS – which is a part of the NGS mission. These select CORS sites will serve as the Foundation for the NSRS in the U.S. Hence, they are termed Foundation CORS (FCORS).

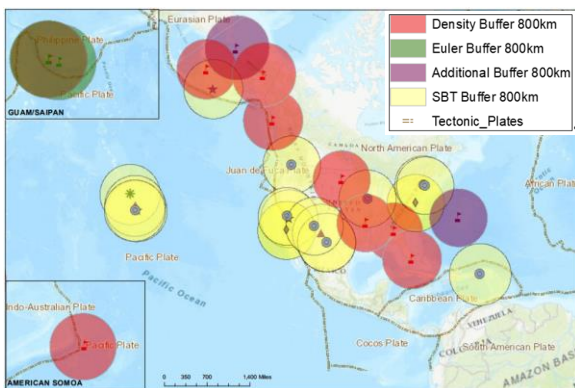


Fig. 2 Prospective sites for Foundation CORS. All circles are 800 km radius and color coded for sites collocated with other space based technique), Euler pole determination, improving spatial density, and additional sites.

c. Euler Pole Parameters

Selection of the FCORS sites is critical as they provide the tie into the ITRF solutions. In turn, these sites serve as fiducial control for the preponderance of CORS sites. FCORS sites would be owned and operated by the NGS or NGS will have a specific memorandum in place to govern

their treatment and maintenance. Figure 2 shows the likely candidates for FCORS.

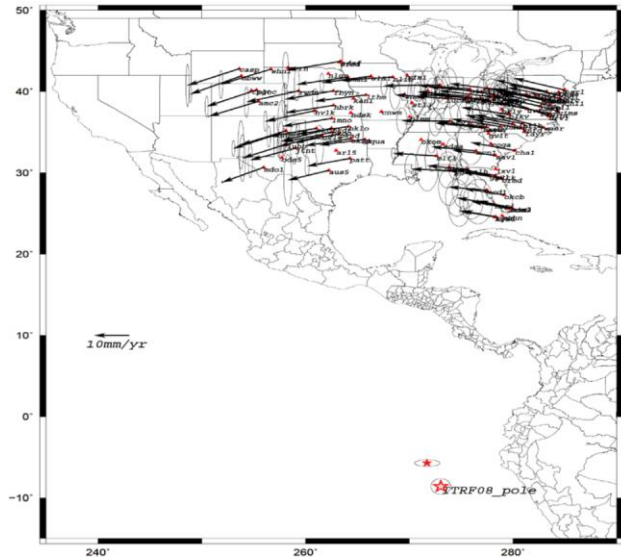


Fig. 3 Euler poles from ITRF 2008 and from a sample test. Changing which sites are included can shift the Euler pole coordinates and rotations significantly.

Several of these FCORS sites will be utilized for determining the Euler pole parameters (EPP). The EPP are the latitude and longitude of the rotation point and the rotation rate around that point. The concept is that most motion in stable plate areas can be described as an angular rotation about a fixed point. It is likely that many CORS will also be utilized in that determination. There are certainly many CORS available for determining NATRF. Selection of which sites to use for this purpose can be difficult. Figure 3 highlights how changing the GNSS sites used in making the Euler pole determination can affect the Euler pole location. The IGS08 solution used a different set of GNSS sites than that for this test case. The offset between the EPP determined from the set of data in Figure 3 and that for the IGS08 would impact position determination at all sites.

Hence, an international working group under the auspices of the North American Reference Frame (IAG SC 1.3c) will convene to determine optimal candidates for determining the EPP. The intent of NATRF is to support positioning throughout all of North America. Other sites will be incorporated such as those from Natural Resources Canada. Similar efforts will also be made in the Caribbean where a different set of issues must be addressed [4].

d. Intra-Frame Velocity Models (IFVM)

The remaining area of concern is the residual velocity in each of these plates. In a larger sense, they are a part of the same problem. If highly accurate positions could be monitored on a periodic basis, then an accurate velocity model could be defined in that same frame. Many countries (e.g., Mexico) plan to adopt this approach, which is essentially a densified ITRF frame. However, for the U.S. case, we will remove most

of the motion with the EPP. The remaining motion within the frame is then the IFVM. This term is adopted because the frame may be extended over a plate boundary. For example in southern California, parts of the state are arguably on the Pacific plate. However, a North American frame would be applied to develop a consistent model over the conterminous United States. This will produce significant residual velocities that must be modeled. Additionally, EPP will not model any vertical motion (e.g., subsidence) at all. Hence, alternative mechanisms are needed to describe the IFVM. Possibilities include gridding the existing CORS network, gridding a densified horizontal and vertical network supplemented by geophysical modeling, and use of Interferometric Synthetic Aperture Radar (InSAR). The next section provides potential solutions for the IFVM.

3. Possible Solutions for the IFVM

a. Gridding CORS

By far, the simplest and cheapest approach would be gridding the extensive U.S. CORS network. NGS just recently completed reprocessing over 20 years of CORS data in order to align with ITRF2014. These data provide both horizontal (Figure 4) and vertical (Figure 5) motions throughout significant portions of the U.S.

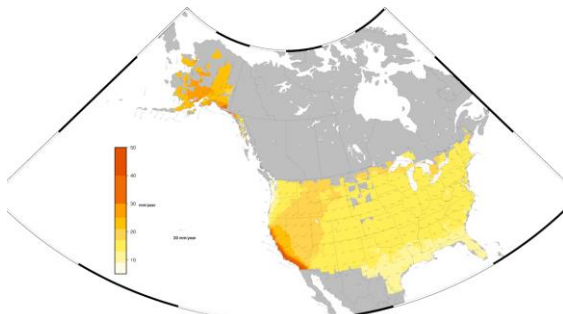


Fig. 4 Horizontal velocities in IGS14 (ITRF2014) frame after reprocessing over 20 years of CORS data. Grey areas lack sufficient data to be resolved.

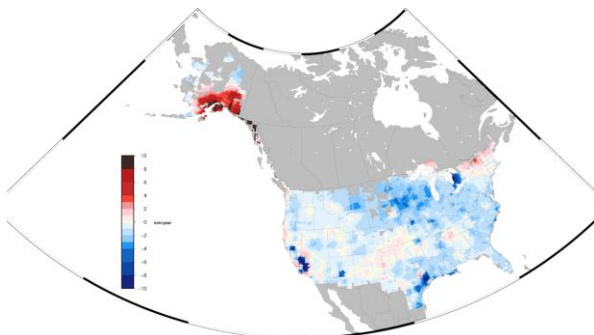


Fig. 5 Vertical velocities in IGS14 (ITRF2014) frame after reprocessing over 20 years of CORS data. Grey areas lack sufficient data to be resolved.

However, this approach will only work if the density of points is equitable, which is not the case. Particularly with

small regions where dynamic activity occurs (e.g., southern California), this approach fails to capture signal in between the control points. There are broader networks of GNSS available outside of the CORS [12,13] that may help improve the reliability of a GNSS-only approach.

b. CORS Plus Geophysical Modeling

Another approach would be to fill in signal between the GNSS control points using geophysical models. Snay et al. [11] produced the Trans4D model to this effect. Others have done likewise. This has the benefit of matching at the GNSS control used to access the reference frame while providing solid geophysical models to describe what happens in between. The control GNSS data constrain the geophysical models. However, the earthquakes and other physical phenomena will require episodic updates to such a model. Hence, it must be maintained regularly.

c. InSAR

The third possibility is the use on InSAR data to map changes in the surface of the Earth over time. This would result in an improved topographic map and associated velocities. Bekaert et al. [3] show how the Hampton Roads region of Virginia was thus modeled and describe the subsidence in the region very well.

The Sentinel-1 satellites [2] are currently online and collecting InSAR data across most of the Earth's surface. These models can help develop a densified ITRF 2014 velocity model, essentially tracking movement anywhere on the Earth. However, some type of service is required to process the InSAR into some velocity model. Additionally, InSAR may not work in all areas. Mountainous regions or swamps are two regions that may be problematic. With the Rocky Mountains in the western U.S. and the southern swamps, this may not be ideal.

In turn, the EPP for each of the four plates would be removed from this ITRF 2014 field to produce a plate specific IFVM. Because they are all defined from the same densified ITRF 2014 model, it would be possible to rotate back through to a common epoch and express coordinates in an adjacent frame (e.g., determine the positions of islands off of California in the PATRF frame instead of the NATRF frame). This would also prevent any discontinuities in the velocity models near the edges of the plates. An IFVM will then account for remaining horizontal velocities and all vertical velocities. The remaining vertical velocities would represent motion in the frame likely tied to crustal deformation. Because an EPP model would only account for the continent-wide horizontal motion, all vertical motion would be expressed by the IFVM.

4. Summary and Outlook

NOAA's National Geodetic Survey continues to progress towards the release of four new frames in 2022 that will be

closely tied to most recent ITRF model at that period, which is likely to be ITRF 2014. They will be exactly aligned a reference epoch - possibly 2020.0. A model of surface velocities will be calculated from InSAR data from Sentinel-1 and other sources in the ITRF 2014 frame.

Euler pole parameters (EPP) will be determined from Foundation CORS and possibly some regular CORS sites on each plate to account for most horizontal motion. These EPP velocities would be removed from the common densified ITRF velocity model to produce a frame-specific set of velocities accounting for any remaining horizontal and vertical motions. The likely solution will be some combination of all with InSAR used in remote regions and GNSS augmented with physical models in more populous regions.

NGS remains committed to delivering these reference frames in conjunction with updated vertical datums from geoid height models in 2022. The expected results of this update of the U.S. National Spatial Reference System is cm-level accurate and precise positioning. This will be two orders of magnitude improvement over the current realizations of the NSRS realized by the North American Datum of 1983 and the North American Vertical Datum of 1988. Furthermore, it will better align the U.S. NSRS with those of other nations in the region and around the world.

References

- [1] Altamimi, Z., P. Rebischung, L. Métivier, and X. Collilieux, ITRF2014: A new release of the International Terrestrial Reference Frame modeling nonlinear station motions, *J. Geophys. Res. Solid Earth*, 121, 6109–6131, 2016, doi:10.1002/2016JB013098
- [2] Attema, E., Davidson, M., Floury, N., Levrini, G., Rosich-Tell, B., Rommen, B., and Snoeij, P., Sentinel-1 ESA's new European SAR mission, *Proc. SPIE 6744, Sensors, Systems, and Next-Generation Satellites XI*, 674403, 17 October 2007, doi: 10.1117/12.747146, <https://doi.org/10.1117/12.747146>
- [3] Bekaert, D. P. S., Hamlington, B. D., Buzzanga, B., Jones, C. E., Spaceborne Synthetic Aperture Radar Survey of Subsidence in Hampton Roads, Virginia (USA), *Scientific Reports*, 7, Article number: 14752, 2017, <https://doi.org/10.1038/s41598-017-15309-5>
- [4] DeMets, C., Mattioli, G., Jansma, P., Rogers, R., Tenorio, C., and Turner, H.L., Present motion and deformation of the Caribbean plate: Constraints from new GPS geodetic measurements from Honduras and Nicaragua, in Mann, P., ed., *Geologic and Tectonic Development of the Caribbean Plate in Northern Central America: Geological Society of America Special Paper 428*, p. 21–36, 2007, doi: 10.1130/2007.2428(02)
- [5] NGS, Ten-Year Strategic Plan 2013–2023, 2013, <https://www.ngs.noaa.gov/INFO/tenyearfinal.shtml>
- [6] NGS, Blueprint Part 1, NOAA Technical Report NOS NGS 62, 2017a, https://geodesy.noaa.gov/PUBS_LIB/NOAA_TR_NOS_NGS_0062.pdf
- [7] NGS, Blueprint Part 2, NOAA Technical Report NOS NGS 64, 2017b, https://geodesy.noaa.gov/PUBS_LIB/NOAA_TR_NOS_NGS_0064.pdf
- [8] NGS, New Datums webpage, 2017c, <https://www.ngs.noaa.gov/datums/newdatums/index.shtml>
- [9] Roman, D.R., The U.S. National Spatial Reference System in 2022, *Proceedings of the FIG Working Week 2017, Helsinki, Finland, May 29–June 2, 2017*, Session TS05C, paper 8841, 2016
- [10] Roman, D.R., United States NSRS 2022: Terrestrial Reference Frames, *Proceedings of the FIG Working Week 2018, Istanbul, Turkey, 06–11 May 2018*, Session TS07E, Paper 9457.
- [11] Snay, R.A., J.T. Freymueller, M.R. Craymer, C.F. Pearson, J. Saleh, Modeling 3-D crustal velocities in the United States and Canada, *JGR*, 121 (7), pp. 5365–5388, 2016, <https://doi.org/10.1002/2016JB012884>
- [12] UNAVCO, Instrumentation Networks, Plate Boundary Observatory (PBO) and COCONet, 2018, <http://www.unavco.org/instrumentation/networks/networks.html>
- [13] UNR-NGL, MAGNET GPS Network, University of Nevada-Reno, Nevada Geodetic Laboratory, 2018, <http://geodesy.unr.edu/magnet.php>

Monitoring of the Church Tower in Herrenberg with Low-Cost GNSS

Li Zhang¹, Iuliana-Madalina Ionescu², Volker, Schwieger¹

Received: September 2018 / Accepted: October 2018 / Published: December 2018
© Journal of Geodesy, Cartography and Cadastre/ UGR

Abstract

The church tower in Herrenberg (nearby Stuttgart) was monitored with leveling to identify the vertical sinking of the church tower. In recent years, some new cracks have been found on the church tower walls which could have been caused by the horizontal deformation of the church tower. To identify the both horizontal and vertical deformation of the church tower, Low Cost GNSS receivers were used. The key limitation factor for accuracy of GNSS (for short baselines) is the multipath effect. Besides, the antenna is very close to the tower walls. For this reason, the influence of the multipath effect will be analyzed and mitigated. Two measurement sessions were realized in May and July 2018, a deformation analysis was done. There are about 5% outliers in the time series, the 3 dimensional standard deviation of single measurement is about 20 mm. After reducing the multipath effect, the 3 dimensional standard deviation of single measurement is improved by about 45%. Deformation analysis shows significant deformation in the north and height component, although there should no significant movement between two sessions, since the movement is very slow and there is only about two months between these two sessions.

Keywords

Low Cost GNSS, Monitoring, Multipath Effect, Deformation Analysis

1. Introduction

Monitoring of artificial structures and natural objects is one of the main tasks of engineering geodesy. Low-Cost single-frequency GNSS receivers are a cost-effective solution compared to traditional geodetic multi-frequency GNSS receivers, particularly for geodetic monitoring tasks where a high number of receivers are applied. Numerous preliminary investigations have shown that Low-Cost single-frequency GPS receivers can achieve similar results as geodetic GNSS receivers (Schwieger and Gläser 2005, Schwieger 2007, Schwieger 2008, Schwieger 2009, Limpach 2009, Glabsch et al. 2010), if the carrier phase measurements of the GNSS receivers are evaluated for short baselines, because the influences of baseline-length-dependent errors, such as ionospheric and tropospheric errors, can be mitigated for short baselines. However, the site-dependent errors, particularly the multipath effects, are the dominant errors of short baselines, particularly in shadowing environment. In practice, it is very often that observation points for GNSS measurements are not selectable, e.g. for the monitoring of high buildings or television towers, where are normally many reflectors there in the antenna vicinity.

The church tower in Herrenberg (nearby Stuttgart in Germany) has a height of about 57 meter and was monitored with leveling to identify the vertical sinking of the church tower. In recent years, some new cracks have been found on the church tower walls which could have been caused by the horizontal deformation of the church tower. To identify both horizontal and vertical deformation of the church tower, Low Cost GNSS receivers can be used. There is only one pillar close to the tower walls which can be used for the GNSS measurement. This means that the multipath could heavily affect the accuracy of the measurement.

Two sessions of GNSS measurements were carried out, the multipath effect was investigated and results of the deformation analysis will be shown in this paper.

2. Test Description

In this test, the U-blox C94-M8P Application Board (C94-M8P 2018) which contains two NEO M8P-2 modules is used (one costs about 300€). NEO M8P-2 is a single-frequency

¹ Dr.-Ing. L. Zhang / Prof. Dr.-Ing. V. Schwieger
Institute of Engineering Geodesy / Faculty of Aerospace Engineering
and Geodesy / University of Stuttgart
Address: Geschwister-Scholl-Str. 24D, 70174 Stuttgart, Germany
E-mail: li.zhang@iigs.uni-stuttgart.de /
volker.schwieger@iigs.uni-stuttgart.de

² Dipl.-Ing. I. Ionescu
Faculty of Geodesy / Technical University of Civil Engineering
Bucharest
Address: Bulevardul Lacul Tei 124, Zip code 020396, Bucharest,
Romania
E-mail: ionescuiuliana10@gmail.com

GNSS receiver. It can receive the signals from GPS, GLONASS and Beidou systems. However, it can only receive the signals from two of these systems at the same time, possible combinations are GPS+GLONASS and GPS+Beidou (NEO M8P-2 2018). For the measurements, a low-cost GNSS antenna (about 100€) Tallysman TW3710 (Tallysman, 2018) was used which can receive GPS L1, GLONASS G1 and Galileo E1 as well as Beidou B1.

To reduce the influence of multipath effects, a self-constructed L1-optimized choke ring ground plane is used. In the preliminary research at the IIGS (Institute of Engineering Geodesy), self-constructed L1-optimized choke rings are developed for Trimble Bullet III GPS antennas. The combination of U-blox LEA-6T GPS receivers and this antenna with the L1-optimized choke rings can already reach an accuracy in the range of millimeters which is comparable to geodetic dual-frequency GNSS antennas and receivers (Zhang and Schwieger 2017). However, it should be noted that the choke rings can only reduce most of the multipath signals from the ground but not from vertical reflectors like walls.

As shown in Fig. 1, the antenna was set up next to the tower walls (corner) of Herrenberg church tower. The horizontal distance from the antenna and the walls are about 0.5 m. Due to the close distance to the tower walls and much multipath effect should show dominating influence. The antenna height is about 1.3 m.

SAPOS (Satellitenpositionierungsdienst der Deutschen Landesvermessung) is the German Satellite Positioning Service, its task is to provide accurate and reliable GNSS correction data based on its permanent GNSS reference stations. A VRS (Virtual Reference Station) station which is calculated by SAPOS is taken as reference station for baseline processing, because the three closest SAPOS stations are about 30 to 40 kilometers away from the church tower. The VRS is about 86 m away from the pillar.

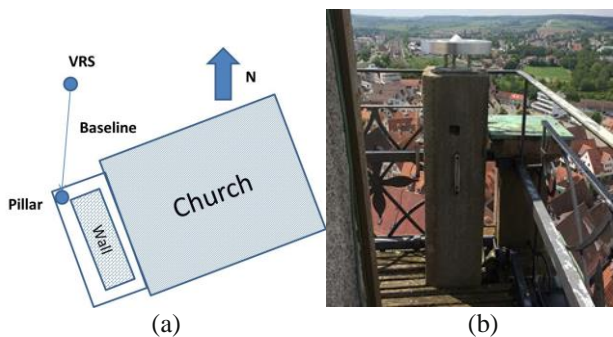


Fig. 1 (a) Sketch and (b) Photo of Test Field

Two sessions of static measurements are carried out. Session 1 is from 17 to 24 May 2018 and session 2 is from 12 to 19 July 2018, so the measurement duration of each of these two sessions is 7 days.

Due to the fact that up to now the SAPOS service only provides GPS and GLONASS data and the satellite availability of GLONASS is better than that of Beidou in Germany, the combination of GPS+GLONASS is chosen for the U-blox receiver. The GNSS raw data are recorded with 1 Hz and stored on a PC, evaluated and post-

processed. The raw data are in UBX binary format and are converted into RINEX format using the RTKLIB (RTKLIB 2018). The VRS and the antenna on the church tower are taken as reference and rover stations respectively for baseline processing baselines. The baseline is processed by software Wa2 provided by Wasoft (Wasoft 2018).

3. Results and Analysis

3.1 Quality Analysis

The results of Wa1 are the baselines in the UTM-system in east, north and height for every second. The outliers in the coordinate's time series, which are probably caused by the unfixed ambiguities, are detected according to the 3σ -rule. Then they are linear interpolated, and the standard deviations are calculated. The percentage of outliers and the standard deviation are regarded as parameter for describing the reliability and accuracy of the measurements, respectively, and reliability and accuracy are two parameters to describe the quality of the GNSS measurement (Zhang 2016). As there is no significant difference between the results within one session (seven days), only the results of the first day of each session will be presented in this paper. Table 1 and Table 2 show the reliability and accuracy of the first day of the two sessions. There are both about 5% outliers in the time series. The standard deviation is about 8 mm and 16 mm in horizontal and vertical direction, so the 3-dimensional standard deviation is about 20 mm. Since the antenna is very close to the tower walls and the multipath effect as mentioned before is dominating, this quality is generally understandable. The measurement quality is worse than that of the test in Zhang (2016), the percentage of the outliers is about 2% and the 3-dimensional standard deviation is about 11 mm. The main reason is that the antenna in Zhang (2016) is about 5 meters away from the main reflector.

Table 1 Reliability of Measurement

Session	Percentage of Outlier [%]			
	E	N	h	Mean
1	4.9	4.5	4.3	4.6
2	4.8	4.7	3.5	4.3

Table 2 Accuracy of Measurement

Session	Standard Deviation [mm]			
	E	N	h	Total
1	7.7	8.2	15.9	19.5
2	8.6	8.4	15.7	19.8

3.2 Multipath Effect Analysis

The main reflectors in the antenna vicinity are the ground and the walls in this test. The reflected signal can cause periodic multipath effects on the carrier phase measurement, and the periodic effects or many harmonic oscillations can be also found in the coordinates (Georgiadou and Kleusberg 1988;

Heister et al. 1997). In Insigler (2008), the frequency of multipath on the carrier phase can be estimated for horizontal and vertical reflectors using the equation (1):

$$f_{\delta\varphi}(t) = \frac{2}{\lambda} \cdot \begin{cases} h \cdot \cos E^s(t) \cdot \dot{E}^s(t) & \text{Horizontal} \\ -d \cdot \sin E^s(t) \cdot \dot{E}^s(t) & \text{Vertical} \end{cases} \quad (1)$$

λ is the wavelength (19 cm approximately for the L1-frequency); h and d are the vertical and horizontal distances between the antenna and the reflector. The closer the reflector is located, the longer is the period. E^s and \dot{E}^s are the elevation of the satellite and its change over time (velocity). A satellite with high elevation can cause long and short periodic multipath effects respectively for horizontal and vertical reflectors. The faster the satellite is moving, the shorter is the generated period of the multipath effect. The wavelength is constant for one antenna, the distance h and d does not change so much. However, the elevation of the satellite changes all the time and the velocity of elevation is not constant, either. For this reason, the frequency of multipath effects varies all the time.

Using the mean value of the velocity of the elevation 0.07 mrad/s and equation (1), the period caused by the multipath effects can be calculated. The period caused by the ground should be more than 18 minutes (that means the frequency should be smaller than 0.92 mHz), and that from the tower wall varies from about 45 minutes to about 4 hours (that means the frequency should be between 0.07 and 0.37 mHz). So, totally, the multipath frequency in this test is less than 0.92 mHz. It should be known that these calculated periods or frequencies are only the roughly estimated values, since the satellite velocity is not constant. The multipath effect in this test is reduced by using the algorithm developed in Zhang (2016) which considers the temporal correlation of GNSS coordinates. The multipath frequencies are estimated precisely and iteratively. This algorithm was described in Zhang (2016); since it is not the focus of this paper, it will not be explained in detail in this paper.

Fig. 2 shows the comparison of the residuals of the baseline of one day and after applying the developed algorithm. It is obvious that the periodic oscillations in the original residuals are reduced significantly. Table 3 shows the baseline standard deviation of the first day in each session after applying the developed algorithm. The improvement of the standard deviation is almost 45%. The improvement of the standard deviation by using the developed algorithm is about 50% in Zhang (2016).

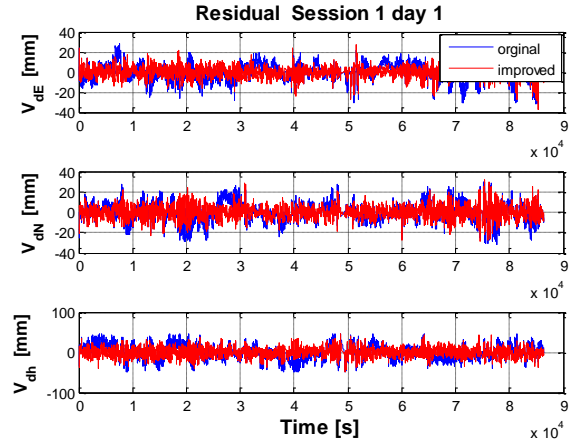


Fig. 2 Coordinates residuals before and after using the algorithm

Table 3 Accuracy of Measurement (after reducing the multipath effect)

Session	Standard Deviation [mm]			
	E	N	h	Total
1	4.1	4.9	8.7	10.8
2	4.2	4.7	8.2	10.3

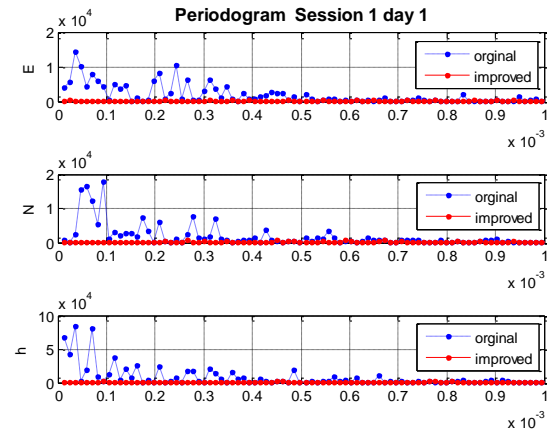


Fig. 3 Periodogram before and after using the algorithm

Fig. 3 shows the periodogram (up to 1 mHz) of coordinates' time series of the baseline on the first day of session 1. The frequencies with high amplitude or energy distribution are mainly between 0 and 0.5 mHz in the periodogram of original residuals (compare Fig. 3). These results match the explained theory very well. Between 0.5 and 0.92 mHz, the amplitude is not high, a possible reason is that multipath signals from the ground were mainly reduced by the self-constructed L1-optimized choke rings; this result is quite similar to the results in Zhang and Schwieger (2017). Furthermore, after applying the algorithm, the high amplitudes are almost disappeared (compare Fig. 3), which leads to the improved results shown in Fig. 2.

3.3 Deformation Analysis

Table 4 shows the mean value of the baseline of the first day in two sessions.

Table 4 Comparison of Baseline in two sessions

Session	Baseline			
	E [m]	N [m]	H [m]	Length [m]
1	15.1643	-43.7118	73.8421	83.1397
2	15.1643	-43.7092	73.8527	83.1474
Diff. [mm]	0.0	-2.6	10.6	10.9

$$t = \frac{d}{s_d} \quad (2)$$

$$s_d = \sqrt{s_{\bar{x}_1} + s_{\bar{x}_2}} \quad (3)$$

$$s_{\bar{x}} = \frac{s_x}{n_{eff}} \quad (4)$$

$$n_{eff} = \frac{n}{1 + \sum_{k=1}^m \frac{(n-k)}{n} K(k)} \quad (5)$$

The differences between the two baselines are 3 mm in north direction and 11 mm in height. A simple deformation analysis can be done by using the t-distribution for each coordinate component (compare equation (2)). The standard deviation of the difference should be calculated by using equation (3). The standard deviation of the mean value of two sessions can be calculated by with the standard deviation of single value and the so-called number of effective observations (compare equation (4)). The reason that the number of effective observations should be used is that the time series is normally temporal correlated. If the number of observations is directly used, the calculated standard deviation of mean value is normally too optimistic (see Heunecke et al. 2013). The number of effective observations can be estimated by using the equation (5). $K(k)$ is the autocorrelation function and m is the normally taken as $n/10$, n is number of observations (Taubenheim 1969).

If the original standard deviation (from Table 2) is taken, the test value is 0, -3.2 and 2.63 for east, north and height component respectively. If the improved standard deviation (from Table 3) is taken for the significant tests the test values will increase, since the numbers of effective observations increase, because the temporal correlation is reduced by using the developed algorithm. So that means if the quantile of 1.96 is taken (with a probability of 95 %), the significant test shows that there is deformation in north and height component. However, there should no deformation between the two days. Since the church tower moves only very slowly, there should be no movement within the two months which is detectable with a GNSS receiver. So, for this reason the data should be analyzed more details in the future. One possible reason could be that the antenna

calibration data is not used (the antenna is not calibrated with the L1-optimized choke rings) and the antenna orientation is not the same in both sessions. And it is assumed that the antenna height is exactly the same, however it is possible that the antenna height is slightly different.

However, it should be kept in mind that the improvement of the measurement accuracy can increase the probability of detection of deformation (see Zhang 2016).

4. Conclusions

In this paper, measurement of the church tower with Low Cost GNSS receivers and its results are shown and analyzed. Since the GNSS antenna is very close to the tower wall, the multipath effect is analyzed intensively. The multipath effect is reduced by the self-constructed L1-optimized choke rings and also by using an algorithm which considers the temporal correlation (see Zhang 2016). The accuracy is improved by about 45% which shows similar results as in Zhang (2016). The significant test shows that there is significant deformation between the two sessions, although there should no significant movement between two sessions, since the movement is very slow and there is about two months between these two sessions. So, in the future, the data of other sessions should be analyzed and more measurement could be done to identify possible deformations of the church tower.

References

- [1] C94-M8P (2018): <https://www.u-blox.com/en/product/c94-m8p>. Last accessed: 28.09.2018.
- [2] Georgiadou, Y.; Kleusberg, A. (1988): On Carrier Signal Multipath Effects in relative GPS Positioning. *Manuscripta Geodaetica*, Band 13, pp. 172–199.
- [3] Glabsch, J.; Heunecke, O.; Pink, S.; Schubäcker, S. (2010): Nutzung von Low-Cost GNSS Empfängern für ingenieurgeodätische Überwachungsaufgaben. In: *GNSS 2010 – Vermessung und Navigation im 21. Jahrhundert*. DVW-Schriftenreihe, Band 63, Wißner-Verlag, Augsburg, pp. 113–129.
- [4] Heister, H.; Hollmann, R.; Lang, M. (1997): Multipath-Einfluß bei GPS-Phasenmessungen: Auswirkungen und Konsequenzen für praktische Messungen. In: *AVN*, Band 5, pp. 166–177.
- [5] Heunecke, O.; Kuhlmann, H.; Welsch, W.; Eichhorn, A.; Neuner, H. (2013): *Auswertung geodätischer Überwachungsmessungen*. 2. Auflage, Wichmann Verlag, Berlin.
- [6] Irsigler, M. (2008): *Multipath Propagation, Mitigation and Monitoring in the Light of Galileo and the Modernized GPS*. Dissertation, Bundeswehr University Munich.
- [7] Limpach, P. (2009): *Rock glacier monitoring with low-cost GPS: Case study at Dirru glacier, Mattertal*. AHORN, Zurich.
- [8] NEO-M8P (2018): NEO-M8P u-blox M8 High Precision GNSS Modules. <https://www.u-blox.com/sites/default/files/NEO->

- [M8P_DataSheet_%28UBX-15016656%29.pdf](#). Last accessed: 28.09.2018.
- [9] RTKLIB (2018): <http://www.rtklib.com/>. Last accessed: 28.09.2018.
- [10] Schwieger, V. (2007): High-Sensitivity GNSS - the Low-Cost Future of GPS?. In: Proceedings on FIG Working Week, Hongkong.
- [11] Schwieger, V. (2008): High-Sensitivity GPS - an availability, reliability and accuracy test. In: Proceedings on FIG Working Week, Stockholm.
- [12] Schwieger, V. (2009): Accurate High-Sensitivity GPS for Short Baselines. In: Proceedings on FIG Working Week, Eilat.
- [13] Schwieger, V.; Gläser, A. (2005): Possibilities of Low Cost GPS Technology for Precise Geodetic Applications. In: Proceedings on FIG Working Week, Kairo.
- [14] Tallysman (2018): http://www.tallysman.com/wp-content/uploads/TW3710_Datasheet_Rev3_6.pdf. Last accessed: 28.09.2018.
- [15] Taubenheim, J. (1969): Statistische Auswertung geophysikalischer und meteorologischer Daten. Akademische Verlagsgesellschaft Geest und Portig, Leipzig.
- [16] Wasoft (2018): <http://www.wasoft.de/>. Last access: 28.09.2018.
- [17] Zhang, L.; Schwieger, V. (2017). Investigation of a L1-optimized choke ring ground plane for a low-cost GPS receiver-system. *Journal of Applied Geodesy*, 12(1), pp. 55-64, 2017. ISSN (Online) 1862-9024, ISSN (Print) 1862-9016, DOI: <https://doi.org/10.1515/jag-2017-0026>.
- [18] Zhang, L.; Schwieger, V. (2016): Improving the Quality of Low-Cost GPS Receiver Data for Monitoring Using Spatial Correlations. *Journal of Applied Geodesy*, 10(2): pp. 119-129. ISSN (Online) 1862-9024, ISSN (Print) 1862-9016, DOI: <https://doi.org/10.1515/jag-2015-0022>.
- [19] Zhang, L. (2016): Qualitätssteigerung von Low-Cost-GPS Zeitreihen für Monitoring Applikationen durch zeitlich-räumliche Korrelationsanalyse, Dissertation at University of Stuttgart.

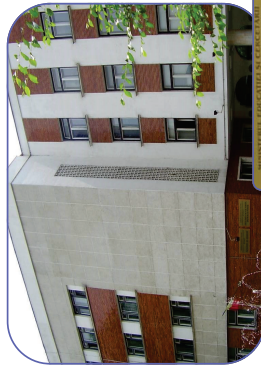
FACULTATEA DE GEODEZIE

<http://geodezie.utcb.ro/>

Facultatea de Geodezie este continuatoarea Școlii de ingineri hotamici din București, înființată în anul 1818 de către Gheorghe Lazăr.

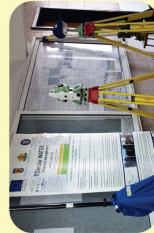
Este o facultate importantă din România, cu o bogată tradiție desfășurată în campusul universitar Tei din București.

Noile tehnologii de măsurare, reprezentare și modelare a spațiului natural și antropic, de gestionare a informației geospațiale, sunt certitudini pentru o profesie de viitor.



Oferta educațională

- Studii universitare de licență, 8 semestre, la specializările:
 - ♦ **Măsurători Terestre și Cadastru,**
 - ♦ **Cadastru și Managementul Proprietăților**
- Studii universitare de masterat, 4 semestre, la specializările:
 - ♦ **Sisteme Informaționale în Cadastru și Publicitate Imobiliară,**
 - ♦ **Planificare Spațială și GIS pentru Dezvoltare Durabilă,**
 - ♦ **Geomatică**
- Studii universitare de doctorat
- Studii postuniversitare de perfecționare
- Cursuri de specializare postuniversitare



**Amintiri
unice
din
PRACTICA**



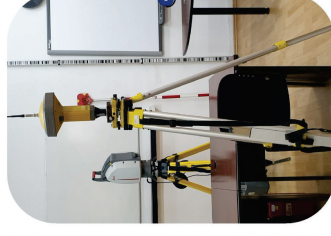
ADMITERE PE BAZA DE DOSAR

iulie / septembrie

locuri finite
de la bugetul de stat

DISCIPLINE STUDIASTE:

- TOPOGRAFIE
- INSTRUMENTE ȘI METODE DE MĂSURARE
- CADASTRU
- GEODEZIE
- CARTOGRAFIE
- SISTEME INFORMATICE GEOGRAFICE
- FOTOGRAMMETRIE
- TELEDETECTIE
- MĂSURĂTORIA GEODEZIE INGINEREȘTI
- ORGANIZAREA TERITORIULUI ȘI URBANISM
- GEODEZIE SPAȚIALĂ
- SISTEME INFORMATICE ÎN MĂSURĂTORI TERESTRE



Fără GEODEZI

- Proprietatea imobiliară nu ar fi garantată...
- Nimic nu se poate construi...
- Nu pot exista hărțile...
- Nu ar exista infrastructură de transport...
- Nu am avea utilități...
- Nu ar fi cadastru...
- Nu am cunoaște poziția în care ne aflăm...
- Nu se poate măsura Pământul...

ROMÂNIA NU SE POATE DEZVOLTA FĂRĂ NOI!



Tri-Axial Accelerometer Calibration for Leveling

Tomas Thalmann, Hans Neuner¹

Received: September 2018 / Accepted: October 2018 / Published: December 2018
© Journal of Geodesy, Cartography and Cadastre/ UGR

Abstract

IMUs (Inertial Measurement Units) are widely used in many robotics applications. Proper calibration is inevitable to ensure usable results in sensor fusion and/or other estimation methods. Numerous sensor models for IMUs can be found in literature. These are investigated from two point of views: How well can the parameters of these models be determined? And how does they influence tilt/inclination estimation with IMUs.

In the first part several sensor models differing in the number of calibration parameters are analyzed in a simulation environment. We investigate two calibration methods: a) multi-position gravity-based calibration method without the need of external equipment, and b) a calibration routine aided by an industrial robot.

In the second part the influence of these calibration parameters on tilt estimation is examined. The well-known leveling equations using accelerometer measurements of gravity for inclination angles determination are used. This method is analyzed using variance based sensitivity analysis to identify important input parameters and to optimize the model/system.

Keywords

MEMS, IMU, Accelerometer, Leveling, Calibration, Sensitivity Analysis, Tilt Estimation

1. Introduction

An IMU (inertial measurement unit) consists of tri-axis accelerometer, tri-axis gyroscopes and sometimes tri-axis magnetometers. A lot of research has been done about IMUs in fields of aerospace, navigation and robotics for several years now. This is because of some unique and beneficial characteristics (compare e.g. [1] or [2]):

- high temporal resolution
- orientation estimation
- high short term accuracy
- unlimited availability due to independence of exterior environment

In the early beginnings of IMU technology it was rather expensive and unhandy in size at the same time [3]. Recent developments of MEMS (Microelectromechanical systems) dramatically reduced size, cost and power consumption [4]. This lead to an even broader scope of applications and also accelerated research [3].

Initially mainly used in navigation tasks, IMUs are now used in several applications: Augmented Reality, Indoor- and Smartphone navigation, Robotics and Mobile Mapping Systems as examples. In particular MEMS IMUs are nowadays used by the geodetic community not only for mobile mapping and navigation tasks. Especially *accelerometer leveling* from gravity sensing attracted interest. Accelerometer leveling means computation two angles roll ϕ_{nb} and pitch θ_{nb} from accelerometer readings of the gravity vector. This method has been used recently for deformation monitoring [5, 6] and frequency analysis of vibrations, e.g. [7, 8].

Another usecase of leveling with MEMS IMUs is tilt compensation of GNSS poles, see [9, 10]. Generally leveling is used in navigation and pose estimation during unaccelerated phase to stabilize attitude and to compensate gyroscope drifts. This direct measurement of the two angles ϕ_{nb} and θ_{nb} is feed into IMU strapdown computation or an integration Kalman Filter.

For all these applications of leveling (based on the acceleration measurements) mentioned here, it is important to know the stochastic model of the derived quantities and to calibrate systematic errors sufficiently. The functional model of leveling is analyzed in terms of variance and sensitivity

¹ Dipl.-Ing. Tomas Thalmann, Univ. Prof. Dr.-Ing. Hans Neuner
FG Ingenieurgeodäsie, Dep.für Geodäsie und Geoinformation
Gußhausstraße 27-29 / E120-5
1040 Wien
Tomas.thalmann@geo.tuwien.ac.at

analysis in Section 3.

A lot of research has focused on sensor and system calibration of IMUs. There are two main questions arising when working on IMU calibration:

- Which error model to use?
- How to calibrate estimate the parameters of the chosen model?

The choice of the inertial instrument error model depends on the application/use-case and on the effect on the derived quantities [11]. This question is tackled in Section 3.

Two basic categories of calibration approaches can be distinguished: **online** and **pre-calibration**. In the first approach, parameters of the IMU error model (see Section 2) are estimated at operation time using sensor fusion (e.g. Kalman filter) with external observations, e.g. GNSS-IMU navigation. The deterministic observability of such state parameters depends on the user dynamics [11], thus is not applicable in static applications. In addition, pre-calibration should be preferred, due to the higher noise level of MEMS sensors:

- possibilities to reduce noise in static environment
- use higher precision external sensors in static environment
- danger of vibrations overlaying systematics in kinematic applications

One has to mention, that at least sensor biases should always be estimated online, since these parameters depend highly on temperature and can significantly change over time [12, 13].

Two groups of pre-calibration methods can be found in literature concerning calibration setup. The first depends on additional equipment like reference sensor (e.g. aviation grade IMU, rate tables [14, 15, 16, 17], or optical 6DOF-tracking [18]) and is generally thought to be executed in the laboratory. These mostly expensive high precision equipment might not be available [19] and is not economical for low-cost MEMS sensors [20]. We summarize these approaches as **equipment-aided** calibrations.

The other group of approaches targets suitable methods for in-field calibration. These should be feasible for end users and mostly rely on Earth's gravity. [21] first introduced the accelerometer calibration using the property: *the magnitude of the static acceleration measured must equal that of the gravity*. This group is referred to as **gravity-based** approaches. Methods based on this property have in common, that gravity \mathbf{g} is measured in multiple quasi-static positions (attitudes). Extensive research has been carried out, differing in number of positions and the underlying estimated error models. A summary can be found in Table 1.

Table 1 Comprehensive summary of related research.

Authors	Model Parameters	# Positions
[21]	Bias and Scale	6
[22, 14, 15, 23]	Bias, Scale and Non-orthogonalities	18

[20]	Bias, Scale, Non-orthogonalities and Cross-axis sensitivities	18 and 24
[17]	Bias, Scale and Non-orthogonalities	9
[24]	Bias, Scale, Nonlinear Scale and Non-orthogonalities	24
[25, 26]	Bias, Scale and Non-orthogonalities	36-50
[19]	Bias, Scale, Non-orthogonalities and Misalignment	30

The disadvantage of gravity-based methods is the required knowledge of the local gravity at an appropriate accuracy level. Because of this and the fact that not all of the above use-cases of accelerometer leveling require exclusively calibrations procedure in-field by user, we analyzed both calibration approaches. For the equipment-aided approach we plan to incorporate an industrial robot as a reference sensor.

The remainder of this paper is organized as follows. In Section 2 several error models for accelerometer triads from literature are introduced. In Section 3 the influence of these estimated error parameters on tilt estimation using accelerometer leveling is analyzed. Based on these results gravity-based and equipment-aided calibrations approaches are compared in Section 4. Section 5 gives the conclusion and outlook.

2. Sensor Models

Several sensor models can be found in literature. They differ mainly in the modeled error parameters. The basic model for the measured accelerometer outputs (measured forces) denoted by $\mathbf{f}^s = [f_x^s \ f_y^s \ f_z^s]^T$ proposed by [21] is:

$$\mathbf{f}^s = \mathbf{S}_f \mathbf{f}^a + \mathbf{b}_f + \mathbf{v}_f, \quad (1)$$

Where $\mathbf{f}^a = [f_x^a \ f_y^a \ f_z^a]^T$ is the calibrated force vector, $\mathbf{b}_f = [b_x \ b_y \ b_z]^T$ is the offset or biases vector and

$$\mathbf{S}_f = \begin{bmatrix} s_x & 0 & 0 \\ 0 & s_y & 0 \\ 0 & 0 & s_z \end{bmatrix} \quad (2)$$

is the scale factor diagonal matrix and \mathbf{v}_f is the accelerometer random noise.

The calibrated forces \mathbf{f}^a refer to the three accelerometer sensitivity axes, thus denoted by \mathbf{a} . Ideally these axes should be orthogonal, but due to imprecise manufacturing this is

most likely not the case. Therefore [14] extended their model to account for this non-orthogonality of the sensor sensitivity axis by introducing

$$\mathbf{f}^b = \mathbf{T}_a^b \mathbf{f}^a, \quad \text{with} \quad \mathbf{T}_a^b = \begin{bmatrix} 1 & -\alpha_{yz} & \alpha_{zy} \\ \alpha_{xz} & 1 & -\alpha_{zx} \\ -\alpha_{xy} & \alpha_{yx} & 1 \end{bmatrix}, \quad (3)$$

which transforms the sensitivity axes to the orthogonal body or IMU-frame (denoted by b) by use of 6 parameters. Here these parameters can be interpreted as “small” angles, where α_{ij} is the rotation of the i -th axis around the j -th body axis, compare Figure 1.

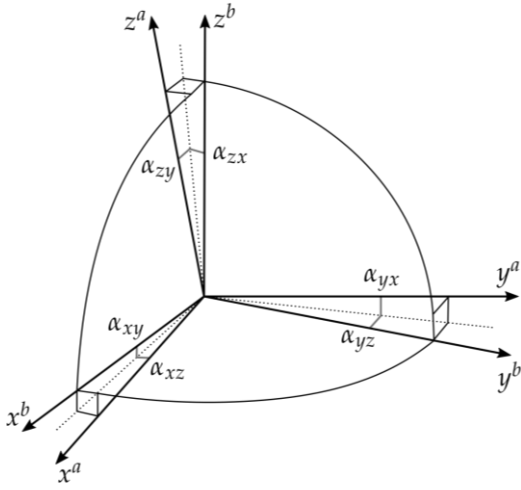


Fig. 1 The non-orthogonal sensitivity axes a can be transformed to the orthogonal body frame b by 6 small angles (after [14]).

Defining the body frame so that the x -axis coincides and y^b -axis lies in the plane spanned by x^a and y^a (3) reduces to:

$$\mathbf{f}^b = \mathbf{T}_a^b \mathbf{f}^a, \quad \text{with} \quad \mathbf{T}_a^b = \begin{bmatrix} 1 & -\alpha_{yz} & \alpha_{zy} \\ 0 & 1 & -\alpha_{zx} \\ 0 & 0 & 1 \end{bmatrix}. \quad (4)$$

This gives a 9-parameter model by extending (1) with (4):

$$\mathbf{f}^s = \mathbf{S}_f \mathbf{T}_a^{b-1} \mathbf{f}^b + \mathbf{b}_f + \mathbf{v}_f, \quad (5)$$

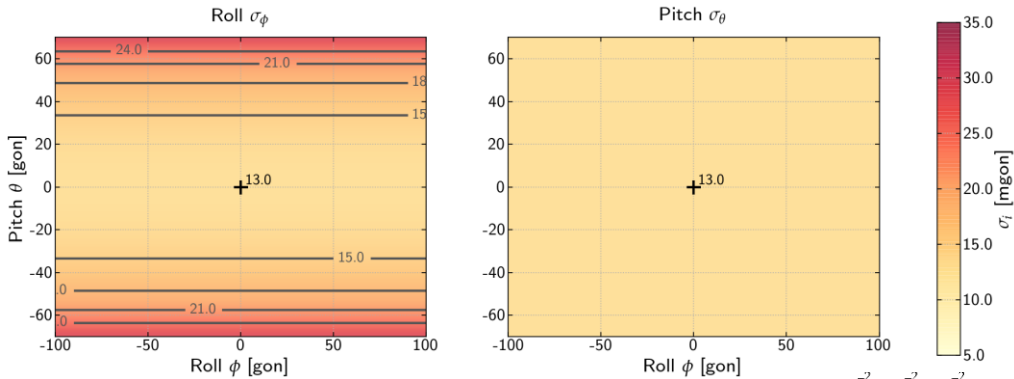


Fig. 2 Accuracy of Roll ϕ_{nb} (left) and Pitch θ_{nb} (right) with uniform accelerometer noise $\sigma_{f_x}^2 = \sigma_{f_y}^2 = \sigma_{f_z}^2$ of $0.002^2 [m^2/s^4]$.

3. Leveling

Following equations are used for accelerometer levelling [3], which describe the orientation of the IMU body frame with respect to the local tangent navigation frame denoted by n . Euler angles are used to describe the attitude using roll ϕ_{nb} , pitch θ_{nb} and yaw ψ_{nb} rotations.

$$\begin{aligned} \phi_{nb} &= \text{atan2}(-f_y^b, -f_z^b) \\ \theta_{nb} &= \text{atan}\left(\frac{f_x^b}{\sqrt{f_y^{b2} + f_z^{b2}}}\right) \end{aligned} \quad (6)$$

Note that $\arctan2()$ must be used for roll computation, but if limiting tilting to the upper half sphere it can be replaced by $\arctan()$.

For this case study we suppose the yaw is exactly known, so $\psi_{nb} = 0$ is used with zero variance throughout the rest of this paper.

The partial derivatives of this model are:

$$\mathbf{F}_{\phi\theta} := \begin{bmatrix} \frac{\partial \phi}{\partial f^b} \\ \frac{\partial \theta}{\partial f^b} \end{bmatrix} = \begin{bmatrix} 0 & \frac{f_z^b}{f_y^{b2} + f_z^{b2}} & \frac{-f_y^b}{f_y^{b2} + f_z^{b2}} \\ \frac{f_{yz}}{f_{yz}^2} & \frac{-f_x^b f_y^b}{f_{yz}^2 f_{yz}} & \frac{-f_x^b f_z^b}{f_{yz}^2 f_{yz}} \end{bmatrix}, \quad \text{with} \quad \begin{aligned} f_{yz} &= \sqrt{f_y^{b2} + f_z^{b2}} \\ f_{xyz}^2 &= f_x^{b2} + f_y^{b2} + f_z^{b2} \end{aligned} \quad (7)$$

3.1. Variance Propagation

In Figure 2 we investigate angle accuracy of roll and pitch with respect to roll and pitch if accelerometer noise is assumed to be equal for all three axis and

This seems a legit assumption for consumer-grade MEMS IMUs, especially $\sigma_{f_b}^2 = 0.002^2 [m^2/s^4]$ predominant static applications where lower measurement rates can be used.

One can see that an accuracy of 13 mgon can be achieved in the vicinity of the zenith direction. Interestingly tilting to the side (producing roll) does not effect both accuracies. On the other hand pitching the pole decreases roll accuracy quadratically.

Figure 3 shows the linear increase of the tilt angle standard deviation with increasing accelerometer noise for a tilted attitude of $\phi_{nb} = 0$ [gon], $\theta_{nb} = 50$ [gon].

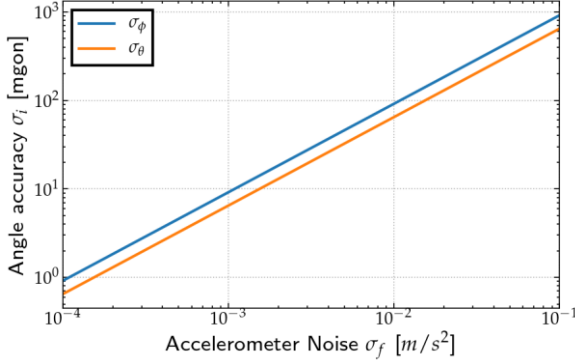


Fig. 3 Tilt angle accuracies with respect to accelerometer noise for $\phi_{nb} = 0$ [gon], $\theta_{nb} = 50$ [gon].

3.2. Sensitivity Analysis

Sensitivity analysis can be used to analyze the relations between input and output parameters of a model [27], in our case $[\phi, \theta] = \varphi(f^b)$. Goals of sensitivity analysis are listed in [27]:

- Model validation,
- Model optimization, and
- Identification of important parameters

These has been ported to the engineering geodesy context by [28] and has been used in many studies since then (e.g. [28, 29, 30]). Please refer to these references for details of the methodology and implementation details. The sensitivity measure S_i^j for the i -th input measure X_i on the j -th output Y_j can be computed using

$$S_i^j = 1 - \frac{\sigma_{E(Y_j|X_{-i})}^2}{\sigma_{Y_j}^2} . \quad (8)$$

Here $\sigma_{Y_j}^2$ describes the variance of the output parameter and $\sigma_{E(Y_j|X_{-i})}^2$ describes the variance of the conditional expectation value, where all input parameters except X_i are fixed.

Considering a parameter free model of $f^s = f^b + v_f$ one can plot the sensitivities/influences of each of the accelerometer measurements on the two output angles ϕ_{nb} and θ_{nb} (s. Figure 4).

The subplots of Figure 4 correspond approximately to the elements of (7). What we can derive from this can be summarized as follows:

- Accelerometer x-axis does not influence ϕ_{nb} computation (compare (6)).
- But is prominent for θ_{nb} for small pitches no matter which ϕ_{nb} .
- Influences of accelerometer measurements on roll computation are independent from pitch.
- For ϕ_{nb} computation f_y is important up to 50 [gon] at which point f_y and f_z are equally important. For higher rolls f_z gains importance.
- For smaller tilt angles < 30 [gon] z-accelerometer reading is inessential for both tilt angles, whilst y-accelerometer is dominant for roll ϕ_{nb} and x-accelerometer is dominant for pitch θ_{nb} computation.

The above conclusions can be verified geometrically and especially the last one can be accounted for in designing calibration schemes.

To get an idea of the importance of the different sensor model parameters when it comes to accelerometer-leveling we have setup a simulation framework, where we can simulate accelerometer measurements according to the models of Section 2. This enables us to perform sensitivity analysis on the 9-parameter model from (5) and the leveling equations (6). The stochastic model has been chosen in accordance to the calibration simulation results from Section 4. Also the simulated quantities are given in Section 4.

Results from the Variance based sensitivity analysis for the

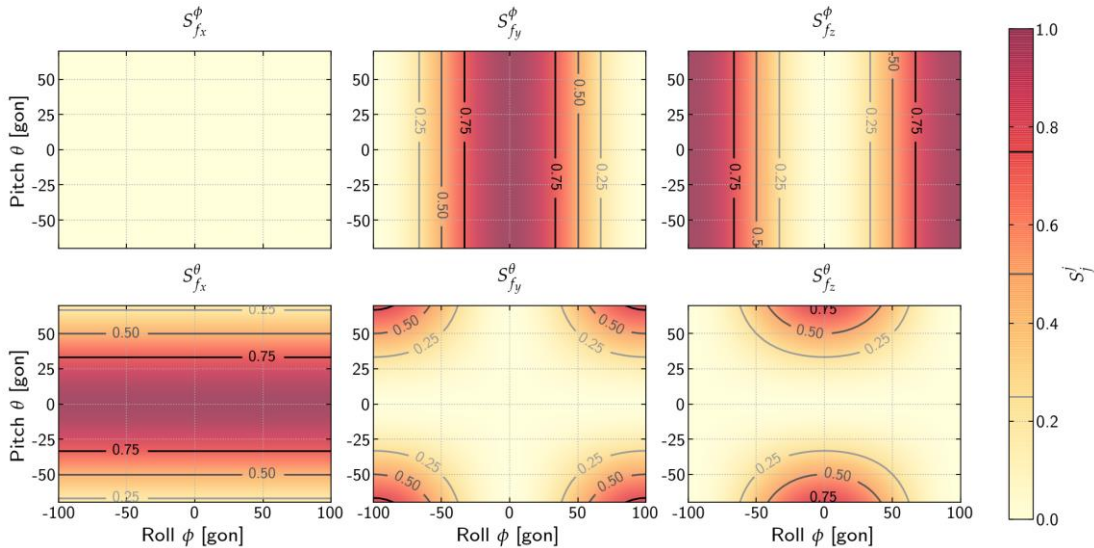


Fig. 4 Total effects of accelerometer measurements f^b for output quantities roll ϕ_{nb} (**upper**) and pitch θ_{nb} (**lower**) with respect to tilt.

9-parameter model (5) are shown in Figure 5 for Roll and in Figure 6 for Pitch at a log scale. Because of the fact that sensitivity quantities are symmetric in both roll- and pitch-axis, only subplots for positive pitches are shown.

As before in Figure 4 we can deduce that the measured forces f_y and f_z in blue are important for roll computation. Moreover the first misalignment parameter α_{zx} in red has a big share on the total variance of ϕ_{nb} . The bias and scale error terms of y and z have an influence of at least one magnitude lower (about 1 to 8%) than the three first listed quantities. The bias shows a quite similar behavior over different ϕ_{nb} and θ_{nb} to the measured forces.

attitudes.

To sum up, scale parameters might be of lowest importance when it comes to accelerometer leveling and special care of misalignment parameters must be taken.

4. Calibration

For the following investigations, the multi-position scheme from [24] is used, where they propose a 24-position calibration scheme. This scheme distributes the measured

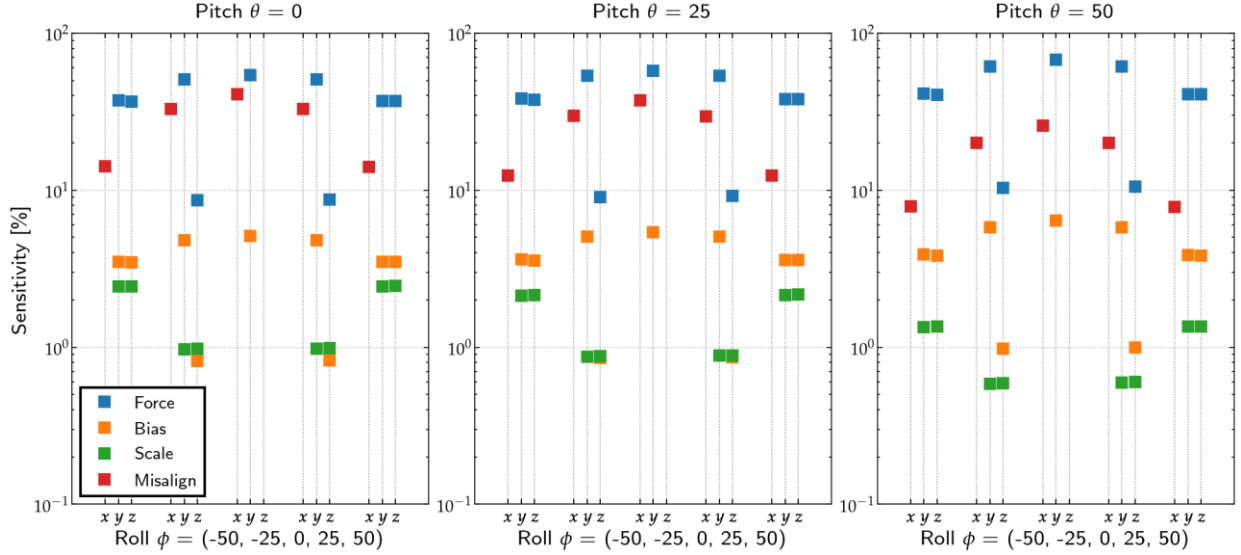


Fig. 5 Effects of all sensor model parameters on Roll ϕ_{nb} .

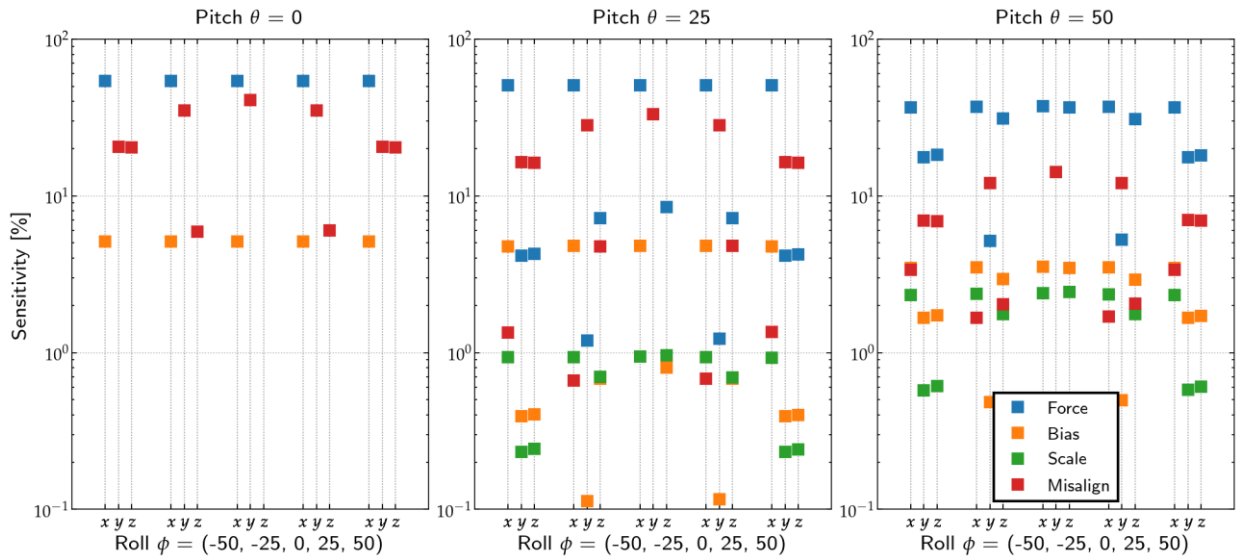


Fig. 6 Effects of all sensor model parameters on Pitch θ_{nb} .

Concerning pitch computation we can see a similar order of importance. After measured forces (and especially f_x) again misalignment parameters (α_{zy} and α_{zx}) are of relevance. Scale parameters stay below 3% for all investigated

g-vector evenly in the unit-sphere. Subsequent simulations are done using the stochastic model from Section 3.1, simulating 2 seconds of data acquisition per attitude and error

parameters of $\tilde{\mathbf{a}}_f = [12 \ 12 \ 44] [mgon]$,
 $\tilde{\mathbf{b}}_f = [0.05 \ 0.01 \ 0.03] [m/s^2]$, and
 $\tilde{\mathbf{s}}_f = [200 \ 200 \ 200] [ppm]$.

4.1. Gravity based

The **gravity-based** approach uses the fact, that the measured gravity must be independent from attitude of the IMU.

$$\varphi(l, \mathbf{x}) = \sqrt{f_x^{b^2} + f_y^{b^2} + f_z^{b^2}} - g = 0 \quad (9)$$

The disadvantage of these approaches as, that g must be known. Generally, no exact measurement of g is available, but values from theoretical models can be computed. Model (9) can be used in a Gauss-Helmert-Adjustment (GH) to estimate the different model parameters of the tri-axial accelerometers of (5).

4.2. Robot aided

Using an industrial robot as additional equipment adds two more observations from robot encoders ϕ_r and θ_r with a standard deviation of 3.2 [mgon].

$$\varphi(l, \mathbf{x}) = \begin{bmatrix} \text{atan}_2(f_y^b, -f_z^b) - \phi_r \\ \text{atan}\left(\frac{f_x^b}{\sqrt{f_y^{b^2} + f_z^{b^2}}}\right) - \theta_r \\ \sqrt{f_x^{b^2} + f_y^{b^2} + f_z^{b^2}} - g \end{bmatrix} = \mathbf{0} \quad (10)$$

The degree of freedom does not change, since two observations and two equations are added to the model per position/attitude.

Comparing these two approaches using simulation, we can see the biggest advantage on determination of misalignment parameters (see Figure 7). Expected bias accuracy is reduced by about 50%, Scale accuracy by about 30% and Misalignment by about 70%. Considering the value of scale parameters of 200 [ppm] and the standard deviation a-posteriori we can deduce that scale parameters are poorly determinable. Additional equipment only with reference attitude measurements can not improve this situation. The biases can be very well estimated, since σ_b is about two orders of magnitude smaller than the simulated true values. For the misalignment parameters we can see very high estimation errors (and corresponding standard deviations) for the gravity based approach. This is were the biggest benefit of additional reference tilting measurements can be seen.

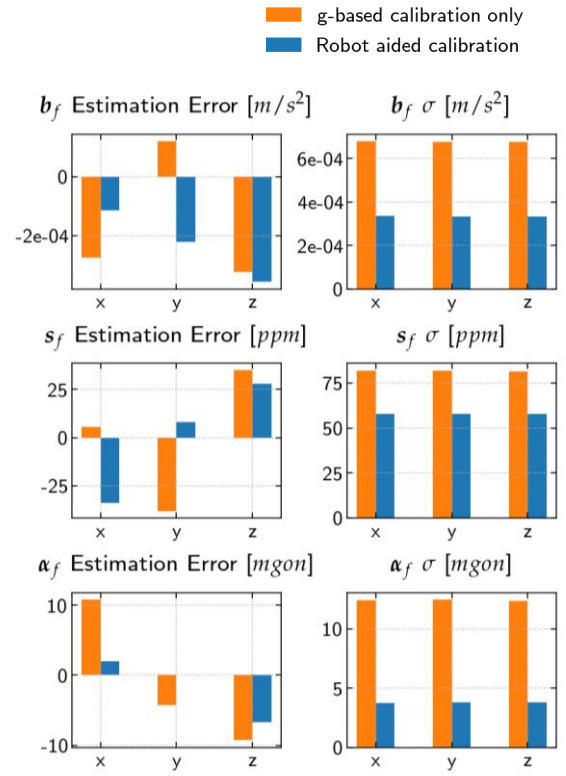


Fig. 7 Comparison of the two IMU calibration approaches. On the (left) printed are the estimation errors from one simulation. On the (right) are the standard deviations of parameters from GH-adjustment.

The correlation structure of the estimated error parameters for both approaches is shown in Figure 8. The estimated parameters of the gravity-based approach are already nearly uncorrelated. This is due to the evenly designed multi-position scheme. Only the scale parameters are correlated by about 0.2. This correlation can be reduced by one order of magnitude using the robot-aided calibration.

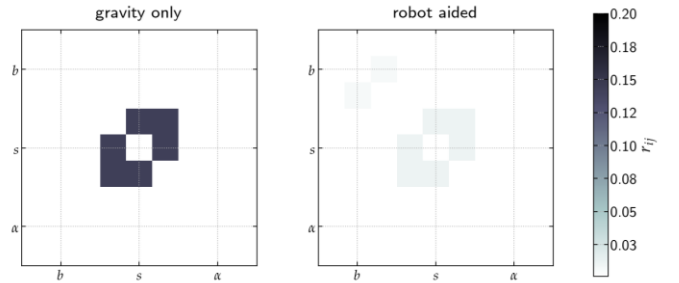


Fig. 8 Correlation Coefficient matrices $\text{abs}(\text{corr}(\Sigma_{xx})) - I$ of the parameters for gravity based (left) and robot aided (right) calibration simulation.

5. Conclusion and Outlook

A simulation framework has been set up to simulate tri-axial accelerometer data according to the different sensor models found in literature. Using this simulation framework, we have first analyzed how well the two tilting angles roll ϕ_{nb} and pitch θ_{nb} can be determined. For small tilting angles (in the vicinity of zenith direction) an accuracy of 13 mgon can be

achieved if accelerometer with uncertainty of 0.002 m/s (standard deviation) are available, which might be feasible with averaging over static timespan. We found out that pitch accuracy is independent of current roll and pitch and that roll accuracy decreases with growing roll.

Using a 9-parameter sensor model for an accelerometer triad the sensitivity of the tilting angles with respect to these sensor model parameters has been investigated using variance based sensitivity analysis. This method revealed that for smaller tilt angles < 30 [gon] only the measured forces of f_y for roll and f_x for pitch are important. Concerning the 9-parameter sensor model the first misalignment parameter α_{zx} show the biggest influence on roll computation. Based on the calibrations simulation results bias and scale parameters are not that important. A comparable conclusion can be drawn for pitch computation, so in general special care must be taken of the three misalignment parameters of the accelerometer triad sensor model.

As a consequence we have analyzed two accelerometer calibration approaches using the same simulation framework. A gravity-only based calibration approach (which can be applied in-field) has been compared with a calibration process aided by an industrial robot. These two calibration procedures are implemented as a GH-adjustment and the studies shows, that especially for those misalignment parameters an aided calibration in laboratory brings an improvement of about 70%.

Future steps would be to test calibration procedures with real hardware. Furthermore, an evaluation experiment for tilt estimation using MEMS IMU should be designed. An idea could be to use the acquired knowledge from sensitivity analysis to optimize the calibration process in terms of economics and time saving. In combination with a recursive least squares approach one might relax the position scheme and adjust it to the given needs. Findings from variance propagation and sensitivity analysis might be used in further studies on pole tilt estimation and compensation both for total stations and GNSS.

References

- [1] Jekeli, C. (2012). Inertial navigation systems with geodetic applications. Walter de Gruyter.
- [2] Hofmann-Wellenhof, B., Legat, K., & Wieser, M. (2011). Navigation: principles of positioning and guidance. Springer Science & Business Media.
- [3] Jekeli, C. (2012). Inertial navigation systems with geodetic applications. Walter de Gruyter.
- [4] Alam, F., Zhaihe, Z., & Jiajia, H. (2014). A Comparative Analysis of Orientation Estimation Filters using MEMS based IMU. 2nd International Conference on Research in Science, Engineering and Technology (ICRSET'2014), 86–91.
- [5] Wilczyńska, I., & Ćmielewski, K. (2016). Modern measurements techniques in structural monitoring on example of ceiling beams. In Proceedings of the 3rd Joint International Symposium on Deformation Monitoring (JISDM), Vienna, Austria (Vol. 30).
- [6] Sekiya, H., Kinomoto, T., & Miki, C. (2016). Determination method of bridge rotation angle response using MEMS IMU. Sensors (Switzerland), 16(11), 1–13. <https://doi.org/10.3390/s16111882>
- [7] Engel, P., Foppe, K., & Köster, U. (2018). Multisensorsystem zur Erfassung von Turmschwingungen an der Marienkirche Neubrandenburg. In MST 2018 - Multisensortechnologie: Low-Cost Sensoren im Verbund, DVW-Schriftenreihe, Band 92 (pp. 167–168). Augsburg.
- [8] Kargoll, B., Omidalizari, M., Loth, I., Paffenholz, J.-A., & Alkhatib, H. (2018). An iteratively reweighted least-squares approach to adaptive robust adjustment of parameters in linear regression models with autoregressive and t-distributed deviations. Journal of Geodesy, 92(3), 271–297.
- [9] Luo, X., Schaufler, S., Carrera, M., & Celebi, I. (2018). High-Precision RTK Positioning with Calibration-Free Tilt Compensation High-Precision RTK Positioning with Calibration-Free tilt Compensation. In FIG Congress 2018 - Embracing our smart world where the continents connect.
- [10] Viney, I. T., & Jackson, P. R. (1999). Method and apparatus for precision location of GPS survey tilt pole. Google Patents.
- [11] Groves, P. D. (2013). Principles of GNSS, inertial, and multisensor integrated navigation systems. Artech house.
- [12] Gleason, S., & Gebre-Egziabher, D. (2009). GNSS applications and methods. Artech House.
- [13] Wendel, J. (2011). Integrierte Navigationssysteme. Oldenbourg Verlag München.
- [14] Skog, I., & Händel, P. (2006). Calibration of a MEMS inertial measurement unit. Signal Processing, 17–22.
- [15] Syed, Z. F., Aggarwal, P., Goodall, C., Niu, X., & El-Sheimy, N. (2007). A new multi-position calibration method for MEMS inertial navigation systems. Measurement Science and Technology, 18(7), 1897–1907. <https://doi.org/10.1088/0957-0233/18/7/016>
- [16] Torayashiki, O., & Komaki, K. (2007). Inertial Sensors. Reliability of MEMS, (December), 205–223. <https://doi.org/10.1002/9783527622139.ch7>
- [17] Zhang, H., Wu, Y., Wu, W., Wu, M., & Hu, X. (2010). Improved multi-position calibration for inertial measurement units. Measurement Science and Technology, 21(1), 015107. <https://doi.org/10.1088/0957-0233/21/1/015107>
- [18] Kim, A., & Golnaraghi, M. F. (2004). Initial calibration of an inertial measurement unit using an optical position tracking system. Position Location and Navigation Symposium, 2004. PLANS 2004, 96–101.
- [19] Lv, J., Ravankar, A. A., Kobayashi, Y., & Emaru, T. (2017). A method of low-cost IMU calibration and alignment. SII 2016 - 2016 IEEE/SICE International Symposium on System Integration, 373–378.
- [20] Fong, W. T., Ong, S. K., & Nee, a Y. C. (2008). Methods for in-field user calibration of an inertial

- measurement unit without external equipment. *Measurement Science and Technology*, 19(8), 085202. <https://doi.org/10.1088/0957-0233/19/8/085202>
- [21] Lötters, J. C., Schipper, J., Veltink, P. H., Olthuis, W., & Bergveld, P. (1998). Procedure for in-use calibration of triaxial accelerometers in medical applications. *Sensors and Actuators, A: Physical*, 68(1–3 pt 2), 221–228.
- [22] Shin, E. H., & El-Sheimy, N. (2002). A new calibration method for strapdown inertial navigation systems. *Zeitschrift Für Vermessungswesen*, 127(1), 41–50.
- [23] Qureshi, U., & Golnaraghi, F. (2017). An Algorithm for the In-Field Calibration of a MEMS IMU. *IEEE Sensors Journal*.
- [24] Cai, Q., Song, N., Yang, G., & Liu, Y. (2013). Accelerometer calibration with nonlinear scale factor based on multi-position observation. *Measurement Science and Technology*, 24(10). <https://doi.org/10.1088/0957-0233/24/10/105002>
- [25] Pretto, A., & Grisetti, G. (2014). Calibration and performance evaluation of low-cost IMUs. 18th International Workshop on ADC Modelling and Testing.
- [26] Tedaldi, D., Pretto, A., & Menegatti, E. (2014). A robust and easy to implement method for IMU calibration without external equipments. In *Robotics and Automation (ICRA), 2014 IEEE International Conference on* (pp. 3042–3049).
- [27] Saltelli, A., Tarantola, S., Campolongo, F., & Ratto, M. (2004). *Sensitivity Analysis In Practice*. John Wiley & Sons.
- [28] Schwieger, V. (2007). Sensitivity analysis as a general tool for model optimisation – examples for trajectory estimation. *Journal of Applied Geodesy*, 1(1), 27–34. <https://doi.org/10.1515/jag.2007.004>
- [29] Ramm, K. (2008). Evaluation von Filter-Ansätzen für die Positionsschätzung von Fahrzeugen mit den Werkzeugen der Sensitivitätsanalyse. Universität Stuttgart.
- [30] Beetz, A. (2012). Ein modulares Simulationskonzept zur Evaluierung von Positionssensoren sowie Filter- und Regelalgorithmen am Beispiel des automatisierten Straßenbaus. Universität Stuttgart.

Solar potential assessment and its feasibility using semi-automatic feature extraction and pyranometer for smart cities

Mudit Kapoor¹, Rahul Dev Garg²

Received: September 2018 / Accepted: October 2018 / Published: December 2018
© Journal of Geodesy, Cartography and Cadastre/ UGR

Abstract

The over-exploitation of non-renewable resources for energy demands is a serious issue. Convergence towards renewable resources such as solar energy is need of the day. Solar energy is the cleanest form of energy available on Earth. The objective of this research is to extract the building rooftop from the satellite images using a k-means clustering algorithm to identify the usable area for solar potential assessment. The scenes of WorldView-3 and Google Earth are segmented into nine parts and the algorithm implemented in Matlab is applied to the individual parts for better utilization of computing resources. This approach has been applied to the Har Ki Pauri, Haridwar that is situated in the northern part of India for solar potential assessment in a fast and accurate manner. The Global Horizontal Irradiance (GHI) data obtained from the database of National Renewable Energy Laboratory (NREL), United States have been used in the solar potential assessment. The validation of the solar potential obtained has been performed using pyranometer data. For the validation purpose, the above-mentioned algorithm has been compared with the digitization in QGIS software. The results obtained from the above-mentioned algorithm developed have extracted 85% to 90% of the features in the satellite image. The developed algorithm has given best results with the WorldView-3 (high-resolution image) than the other coarser resolution scenes. The developed approach is helpful in evaluating the feasibility of the large areas for solar potential assessment. This methodology is useful for the implementation of different government's solar energy generation schemes for rural and hilly areas. It helped in estimating the solar potential of the large hilly area for electricity generation.

This approach is useful for a larger area as it computes the usable area by dividing the scenes into smaller parts and applies the algorithm individually to each part of the scene.

Keywords

k-means clustering, GHI, rooftop, solar potential, Google Earth, WorldView-3

1. Introduction

Remote Sensing is helping us in many applications such as feature extraction, classification, etc. Satellite images of various resolutions are available through many remote sensing satellites. The satellite images are of different resolutions that range from some centimeter to meters. Centimeter level resolution images are known as high resolutions images. High-resolution images contain the information of easily extractable features such as rooftops, buildings, roads, and trees. Therefore these high-resolution images have been used by many researchers to extract rooftops using segmentation, image processing techniques, remote sensing, and Geographic Information System (GIS) analysis [1]–[5].

In the early stage of Geomatics, feature extraction has been performed using manual digitization process [6], [7]. This is not only an accurate method of feature extraction from the satellite images but also highly skilled manpower is needed for the same.

Rayleigh scattering and aerosols play an important role in determining the solar irradiance reaching the Earth's surface. Most of the energy radiations coming from the Sun are in the wavelength range of 300 nm to 2400 nm as shown in Figure 1 [8]–[10]. Solar irradiance has been analyzed and predicted by many researchers to predict solar potential available at the location [11], [12]. The best way to convert the solar energy into electricity is through Solar Photovoltaic (SPV) panels [4], [5], [13]–[16].

Pyranometer has been utilized to predict the solar potential of the small and large area for solar plant feasibility studies [13], [14]. The pyranometer data provides the validation of the predicted and calculated Global Horizontal Irradiance

¹Ph.D. Candidate, M.Tech. Mudit Kapoor

²Associate Professor, Ph.D. Rahul Dev Garg
Geomatics Engineering Group, Civil Engineering Department,
Address: Indian Institute of Technology Roorkee-247667,
Uttarakhand, India
E-mail: mkapoor@ce.iitr.ac.in, garg_fce@iitr.ac.in

(GHI) values [13]. In this study, the pyranometer data has been used to compare the results obtained using GHI data from National Renewable Energy Laboratory (NREL), United States [17]–[20]. The pyranometer used in this study works in the wavelength range of 305 nm to 2800 nm.

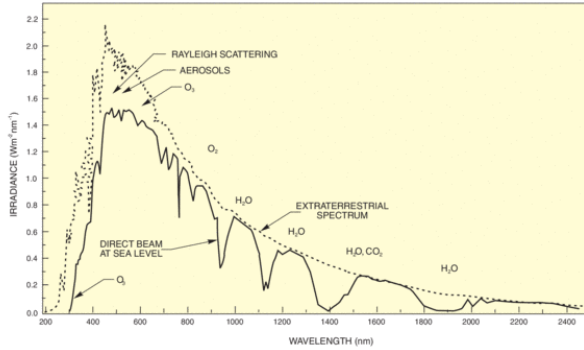


Fig. 1 Solar irradiance enters into the Earth's atmosphere. The dotted line shows extraterrestrial irradiance [21]

The rest of the paper is organized into four sections. The study area has been shown in section 2. Methodology and its flowchart are described in section 3. Results have been shown in section 4 with a discussion about the results obtained. Conclusions of this study have been analyzed in section 5 with future scope for related studies.

2. Study area

Har Ki Pauri has been selected as the study area for this study (Figure 2). This place is located in the holy city of Haridwar, Uttarakhand, India [22]. The central coordinates of this location are latitude 29.958506°, longitude 78.172681°, and altitude 286m [23]. The area and perimeter of the study area are 276142 m² and 2061 m respectively. Socioeconomic data has been used to estimate the energy requirement of the study area [24].

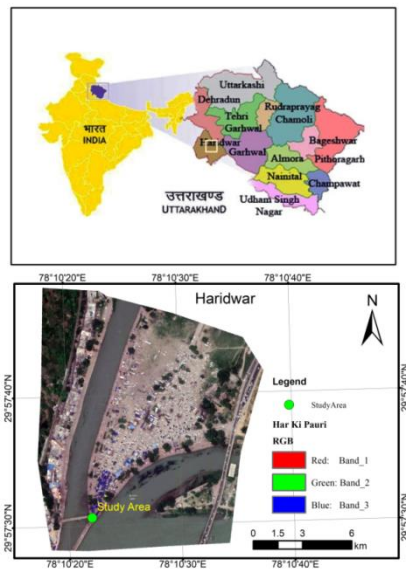


Fig. 2 Study area selected for this study

3. Methodology

Semi-automatic rooftop extraction approach has been applied to assess the solar potential of the selected study area described in the previous section (Figure 3). High-resolution satellite images of this study area have been downloaded from the Google Earth and SGIS tools [23], [25]. Complete study area in high-resolution images is too big to process the k-means clustering algorithm on it using processor i7 (8th generation) and 8GB RAM. It is recommended from this study that segmentation is a good approach to process the larger area for the k-means clustering algorithm. Therefore this study area has been divided into nine parts for algorithm processing. Image segmentation has been performed to segment it into nine parts.

Blue coloured rooftops of the selected study area have been extracted using k-means clustering shown in algorithm 1. This semi-automatic approach algorithm has been utilized to extract rooftops in the Matlab programming environment [26].

Algorithm 1: k-means clustering [27]

- Input the coloured image (jpg format)
- Convert the image to RGB to L*a*b* color space
- Apply k-means algorithm to classify the colours in a*b* space
- Tag the pixels using k-means results
- Images have been produced using segments of H&E colours
- The result is a segmented image

K-means clustering algorithm has been performed on the individual part to extract blue coloured rooftops for usable area calculation. The algorithm has been implemented using Matlab on each segmented part of the study area to extract rooftops. Out of the nine-segmented parts, seven parts contain the rooftop information. These segmented parts then combined together to analyze the complete usable area available for solar potential assessment. This algorithm has extracted almost most of the blue coloured rooftops at this location. The value of the usable area has been calculated using high-resolution satellite imagery mosaic and GIS analysis in ArcMap 10.3 [28].

GHI from NREL has been obtained to assess the solar potential assessment on the rooftops at Har Ki Pauri, Haridwar. This GHI has been converted into the tilted GHI for utilizing the maximum solar irradiance falling on the SPV panels [29]. An algorithm has been implemented using Perl programming language to convert GHI (H) into tilted GHI (H_T). Equation 1 has been utilized to convert GHI into tilted GHI. H_b, H_d, and H_r are the beam, diffuse and reflected irradiance respectively used for this study. The tilt factors for the beam, diffuse, and reflected irradiance are R_b, R_d, and R_r respectively.

$$H_T = H_b R_b + H_d R_d + H_r R_r \quad (1)$$

Researchers have mentioned 10-15% of uncertainty in the satellite-based GHI calculation [30]. Pyranometer data have been utilized for solar potential assessment for this study. Instantaneous GHI values from pyranometer have been used to calculate solar potential at an instance for validation purpose. Pyranometer readings have been analyzed to predict the solar potential at an instance for this study. The outputs of this pyranometer are GHI (W/m^2) and Daily Horizontal Irradiance (Wh/m^2). GHI is the sum of the diffuse and beam irradiances [8], [15], [31]. In this pyranometer, GHI has been

calculated using equation 2 mentioned below[32].

$$E_e = \text{DDP}/S \quad (2)$$

E_e = Irradiance (W/m^2)

DDP = Multimeter has been used to calculate the potential difference (μV)

S = Constant used in this equation i.e. $15.20 \mu\text{V} (\text{W/m}^2)$

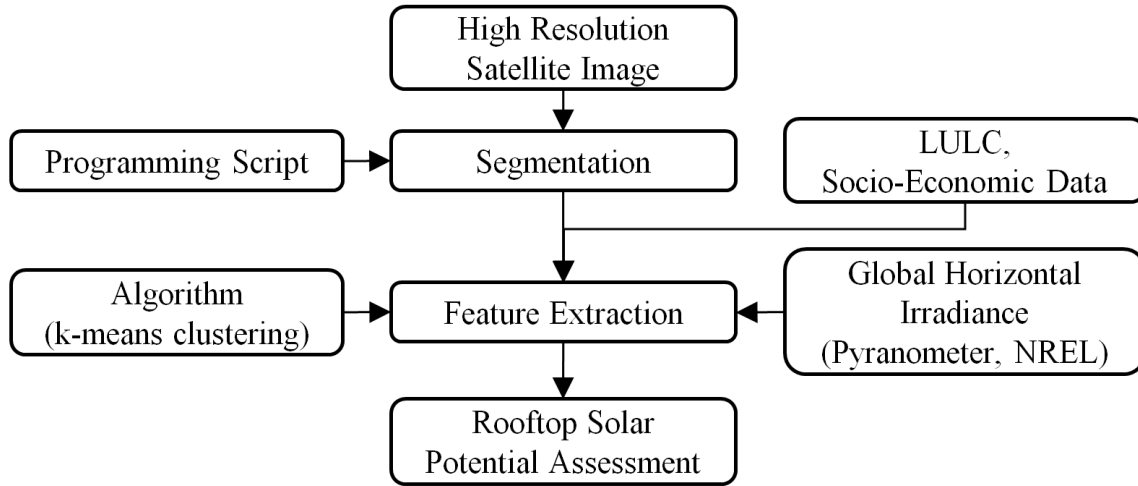


Fig. 3 The methodology adopted for the study

4. Results

It has been found from the results that almost 90% of the rooftops have been extracted using a k-means clustering algorithm (Figure 4). It has been found from the results that out of nine segmented parts, seven parts contain the rooftop information.

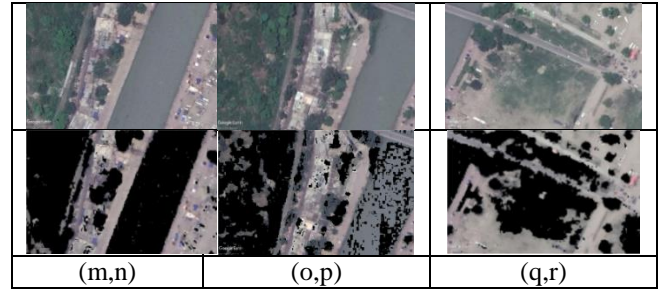
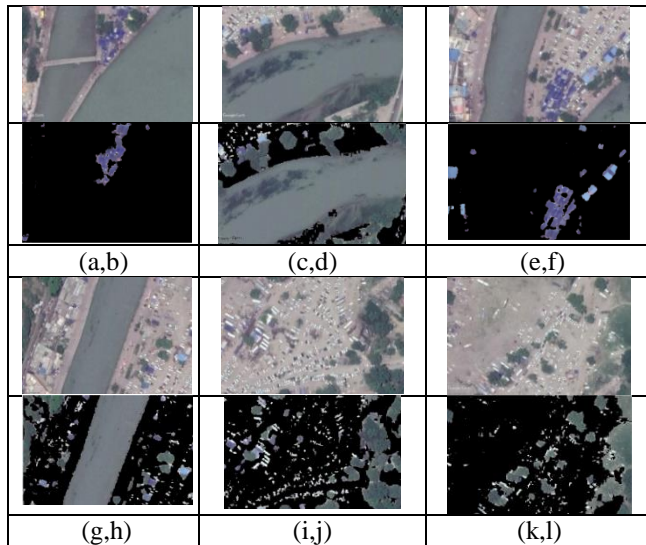


Fig. 4 (a to r) (a) Segmented part of the study area and (b) Extracted rooftops using semi-automatic rooftop extraction approach applied on nine segmented parts, respectively

The complete rooftop areas of the study area have been developed by combining the outputs of the semi-automatic rooftop algorithm (Figure 5). This figure shows the extracted blue coloured rooftops. The shape, colour, size, and texture information have been used to identify the features as rooftops. GIS technology and outputs have been analyzed in ArcMap 10.3 to calculate the value of the rooftop's area for SPV installations (Figure 6). The total rooftop area for this study is 4228 m^2 . Parameters such as SPV infrastructure and maintenance have been taken into consideration for the usable areas to install the SPV panels. This usable area is the actual calculated area after taking care of all the parameters described above. Therefore out of the total rooftop area, 85% i.e. 3594 m^2 has been considered for solar potential assessment.

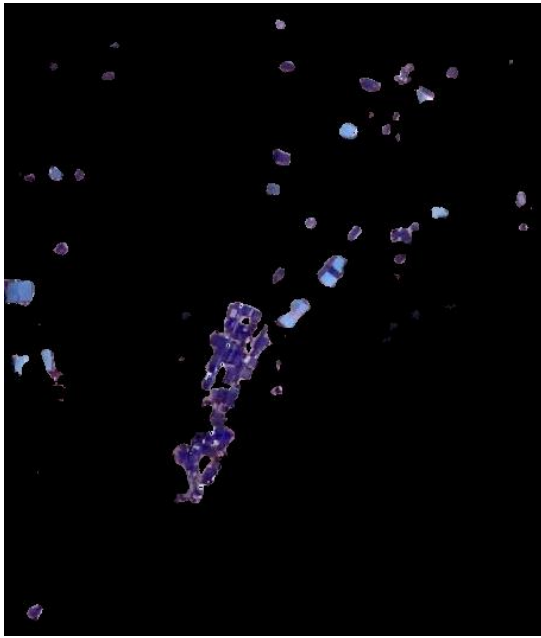


Fig. 5 Extracted rooftops over the complete study area selected for this study

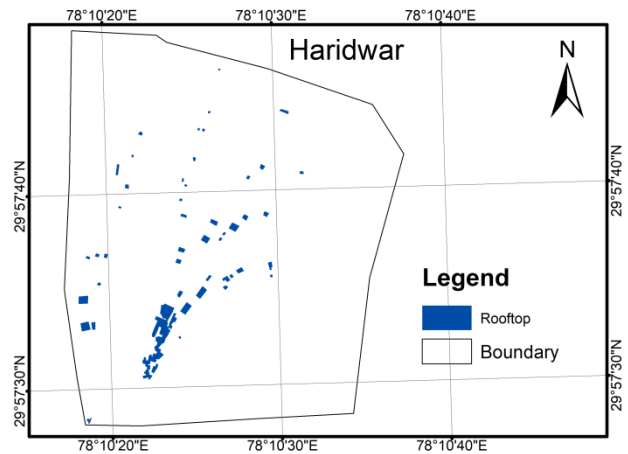


Fig. 6 Rooftops extracted using GIS analysis for usable area calculations

The parameters such as GHI, tilted GHI, and tilt angle considered for solar potential assessment in this study are shown in Table 1. The average monthly solar potential assessed is 20.8413 MW

Table 1 Solar potential assessment over Har Ki Pauri rooftops

Year	Month	GHI (kWh/m ² /day)	Tilt Angle (degree)	Tilted GHI (kWh/m ² /day)	Solar Potential (MWh)
GHI Average Data 2002- 2008	January	3.284	19.96	4.175	15.005
	February	4.433	19.96	5.286	18.998
	March	5.889	19.96	6.559	23.573
	April	6.781	19.96	7.100	25.518
	May	7.411	19.96	7.469	26.844
	June	6.516	19.96	6.453	23.192
	July	5.532	19.96	5.510	19.803
	August	5.239	19.96	5.362	19.271
	September	5.317	19.96	5.745	20.648
	October	5.213	19.96	6.104	21.938
	November	4.206	19.96	5.342	19.199
	December	3.406	19.96	4.481	16.105
	Annually	5.270	19.96	7.056	25.360

The value of GHI obtained by pyranometer is 724 Wh/m² (Table 2). This value has been converted into the tilted GHI i.e. 738.74 Wh/m². The solar potential for an instance using pyranometer is 2.655 MW. This value shows it is feasible to install solar potential at this location and also validates the results obtained using tilted GHI data.

Table 2 Solar Potential assessed using pyranometer data (instance)

Date/ Time	GHI (Wh/m ²)	Tilt Angle (degree)	Tilted GHI (Wh/m ²)	Solar Potential (MW)
11-09-18 /14:18:53	724	19.96	738.74	2.655

using India census 2011 data and software tool [24], [33]. The value of total energy consumption for this location is 1.53 MWh (Table 3). This value shows that it is feasible to obtain the required electricity by installing the rooftop solar plant.

Table 3 Energy requirements of the selected study area using India Census 2011 data

#	Houses	Population	Requirement (per capita, kWh)	Total Energy consumption (MWh)
1	70	280	5.46	1.53

Energy requirements for this study area have been calculated

5. Conclusions

The main objective of this study was to estimate the usable area and feasibility study of the solar plant at Har Ki Pauri, India. The semi-automatic feature extraction approach helped in extracting the rooftops. These extracted rooftops along with GIS analysis have been utilized to calculate the rooftop's area. The semi-automatic feature extraction approach helped in extracting approximately 90% of the rooftops. The solar potential assessment and energy requirement analysis of this location showed it is feasible to install SPV panels for electric power generation. GHI from pyranometer at the local level and GHI [NREL] extracted using satellite images have been utilized in this study. In this study, the semi-automatic feature extraction approach has been combined with the feasibility study for solar potential assessment using Big data cloud environment. These types of solar potential assessments help government bodies in smart city policy making and providing subsidies to the people living in the rural or hilly terrains.

The results of this semi-automatic approach can be improved by using higher resolution satellite image for accurate prediction and assessment. Vegetation, trees, shadows have not considered for this study. These parameters can be taken into consideration in related studies.

Acknowledgments

This study has been carried out as a part of the Ph.D. programme. The first author is grateful to the Young Surveyor Grant, International Federation of Surveyors (FIG) for providing financial support.

References

- [1] A. A. F. Husain, W. Z. W. Hasan, S. Shafie, M. N. Hamidon, and S. S. Pandey, "A review of transparent solar photovoltaic technologies," *Renew. Sustain. Energy Rev.*, vol. 94, no. July, pp. 779–791, 2018.
- [2] M. Ghanea, P. Moallem, and M. Momeni, "Automatic building extraction in dense urban areas through GeoEye multispectral imagery," *Int. J. Remote Sens.*, vol. 35, no. 13, pp. 5094–5119, 2014.
- [3] G.- Data, *GIScience Remote Sensing Retrieval of High Resolution Land Surface Temperature Using Landsat 5 TM and.* 2017.
- [4] I. Gherboudj and H. Ghedira, "Assessment of solar energy potential over the United Arab Emirates using remote sensing and weather forecast data," *Renew. Sustain. Energy Rev.*, vol. 55, pp. 1210–1224, 2016.
- [5] R. M. Moharil and P. S. Kulkarni, "A case study of solar photovoltaic power system at Sagardeep Island, India," *Renew. Sustain. Energy Rev.*, vol. 13, no. 3, pp. 673–681, 2009.
- [6] O. Sharma, D. Mioc, and F. Anton, "Polygon feature extraction from satellite imagery based on colour image segmentation and medial axis," *Int. Arch. Photogramm. Remote Sens. Spat. Inf. Sci.*, vol. 37, no. B3a, pp. 235–240, 2008.
- [7] B. Liss, M. D. Howland, and T. E. Levy, "Testing Google Earth Engine for the automatic identification and vectorization of archaeological features: A case study from Faynan, Jordan," *J. Archaeol. Sci. Reports*, vol. 15, no. September, pp. 299–304, 2017.
- [8] A. Kazantzidis, E. Nikitidou, V. Salamalikis, P. Tzoumanikas, and A. Zagouras, "New challenges in solar energy resource and forecasting in Greece," *Int. J. Sustain. Energy*, vol. 37, no. 5, pp. 428–435, 2018.
- [9] Z. Qu *et al.*, "Fast radiative transfer parameterisation for assessing the surface solar irradiance: The Heliosat-4 method," *Meteorol. Zeitschrift*, vol. 26, no. 1, pp. 33–57, 2017.
- [10] M. Taylor, P. G. Kosmopoulos, S. Kazadzis, I. Keramitsoglou, and C. T. Kiranoudis, "Neural network radiative transfer solvers for the generation of high resolution solar irradiance spectra parameterized by cloud and aerosol parameters," *J. Quant. Spectrosc. Radiat. Transf.*, vol. 168, pp. 176–192, 2016.
- [11] X. Zhou, J. Yang, F. Wang, and B. Xiao, "Economic analysis of power generation from floating solar chimney power plant," *Renew. Sustain. Energy Rev.*, vol. 13, no. 4, pp. 736–749, 2009.
- [12] I. Kougias *et al.*, "The potential of water infrastructure to accommodate solar PV systems in Mediterranean islands," *Sol. Energy*, vol. 136, pp. 174–182, 2016.
- [13] C. A. Bode, M. P. Limm, M. E. Power, and J. C. Finlay, "Subcanopy Solar Radiation model: Predicting solar radiation across a heavily vegetated landscape using LiDAR and GIS solar radiation models," *Remote Sens. Environ.*, vol. 154, pp. 387–397, 2014.
- [14] M. A. Martínez, J. M. Andújar, and J. M. Enrique, "A new and inexpensive pyranometer for the visible spectral range," *Sensors (Switzerland)*, vol. 9, no. 6, pp. 4615–4634, 2009.
- [15] C. F. Peruchena and A. F. Amores, "Uncertainty in monthly GHI due to daily data gaps," *Sol. Energy*, vol. 157, no. August, pp. 827–829, 2017.
- [16] Y. Su, "A Comparative Analysis of the Performance of a Grid-Connected Photovoltaic System Based on Low-and High-Frequency Solar Data," *Int. J. Green Energy*, vol. 12, no. 12, pp. 1206–1214, 2015.
- [17] NREL, "Inventory of Solar Radiation / Solar Energy Systems Estimators, Models, Site- Specific Data, and Publications," 2016.
- [18] J. R. Janke, "Multicriteria GIS modeling of wind and solar farms in Colorado," *Renew. Energy*, vol. 35, no. 10, pp. 2228–2234, 2010.
- [19] M. Sengupta, P. Gotseff, M. Sengupta, and P. Gotseff, "Evaluation of Clear Sky Models for Satellite-Based Irradiance Estimates Evaluation of Clear Sky Models for Satellite-Based Irradiance Estimates," no. December, 2013.

- [20] M. Kapoor and D. Bassir, "Climate change for agriculture, forest cover and 3D Urban models," in *International Archives of the Photogrammetry, Remote Sensing and Spatial Information Sciences - ISPRS Archives*, 2014, vol. 40, no. 8, pp. 787–791.
- [21] Newport, "Introduction to Solar Radiation," *Newport Corporation*, 2018. [Online]. Available: <https://www.newport.com/t/introduction-to-solar-radiation>. [Accessed: 01-Sep-2018].
- [22] Wikipedia, *Har Ki Pauri*. Haridwar, 2018.
- [23] Google Earth, "Google Earth," 2018. [Online]. Available: <https://earth.google.com/web/>. [Accessed: 30-Jan-2018].
- [24] Census Population Data, "Haridwar District Population Census 2011, Uttarakhand literacy sex ratio and density," *Census Population Data*, 2015. [Online]. Available: <https://www.census2011.co.in/census/district/586-haridwar.html>. [Accessed: 02-Sep-2018].
- [25] Elshayal, "Elshayal Smart GIS 18.022," 2018. [Online]. Available: <https://freesmartgis.blogspot.com/>.
- [26] Mathworks, "Deep Learning with Matlab," *Introd. Deep Learn. with MATLAB*, p. 15, 2017.
- [27] MathsWorks, "Color-Based Segmentation Using K-Means Clustering - MATLAB & Simulink Example - MathWorks India," *MathsWorks*, 2018. [Online]. Available: <http://in.mathworks.com/help/images/color-based-segmentation-using-k-means-clustering.html;jsessionid=274172036a725ca7bc89020ded9e>. [Accessed: 16-Aug-2018].
- [28] Esri, "ArcGIS 10.3.1 for Desktop quick start guide—Help | ArcGIS Desktop," 2018. [Online]. Available: <http://desktop.arcgis.com/en/arcmap/10.3/get-started/quick-start-guides/arcgis-desktop-quick-start-guide.htm>. [Accessed: 01-Sep-2018].
- [29] S. P. Sukhatme and J. K. Nayak, *Solar Energy: Principles of Thermal Collection and Storage*, Third. New Delhi: Tata McGraw-Hill Education, 2008.
- [30] PV-Tech, "The art and science of pyranometers," *PV-Tech*, pp. 48–51, 2015.
- [31] T. Muneer, X. Zhang, and J. Wood, "Evaluation of an innovative sensor for measuring global and diffuse irradiance, and sunshine duration," *Int. J. Sol. Energy*, vol. 22, no. 3–4, pp. 115–122, 2002.
- [32] DeltaOHM, "LP PYRA 03 - Datasheet." pp. 1–12, 2007.
- [33] M. Kapoor and R. D. Garg, "Cloud computing for energy requirement and solar potential assessment," *Spat. Inf. Res.*, vol. 26, no. 4, pp. 369–379, 2018.

Printed at



servicii de editare și publicare a cărților
gamă completă de tipizate

TIPOGRAFIE | EDITURĂ

Împreună dăm valoare hârtiei!

www.zven.ro | zven.print@gmail.com | tel./fax: 0345 401 330 | mobil: 0765 464 304